Monthly Notices
of the
ROYAL ASTRONOMICAL SOCIETY

MNRAS **438,** 752–767 (2014)
Advance Access publication 2013 December 14

doi:10.1093/mnras/stt2243

New constraints on gamma-ray burst jet geometry and relativistic shock physics

C. Guidorzi,[1⋆] C. G. Mundell,[2] R. Harrison,[2] R. Margutti,[3] V. Sudilovsky,[4] B. A. Zauderer,[3] S. Kobayashi,[2] A. Cucchiara,[5] A. Melandri,[6] S. B. Pandey,[7] E. Berger,[3] D. Bersier,[2] V. D'Elia,[8] A. Gomboc,[9,10] J. Greiner,[4] J. Japelj,[9] D. Kopač,[9] B. Kumar,[7] D. Malesani,[11] C. J. Mottram,[11] P. T. O'Brien,[12] A. Rau,[4] R. J. Smith,[2] I. A. Steele,[2] N. R. Tanvir[12] and F. Virgili[2]

[1]*Department of Physics and Earth Sciences, University of Ferrara, via Saragat 1, I-44122, Ferrara, Italy*
[2]*Astrophysics Research Institute, Liverpool John Moores University, IC2, Liverpool Science Park, 146 Brownlow Hill, Liverpool L3 5RF, UK*
[3]*Harvard–Smithsonian Center for Astrophysics, 60 Garden Street, Cambridge, MA 02138, USA*
[4]*Max–Planck–Institut für extraterrestrische Physik, Giessenbachstrasse 1, D-85748, Germany*
[5]*Department of Astronomy and Astrophysics, UCO/Lick Observatory, University of California, 1156 High Street, Santa Cruz, CA 95064, USA*
[6]*INAF – Osservatorio Astronomico di Brera, via E. Bianchi 46, I-23807 Merate (LC), Italy*
[7]*Aryabhatta Research Institute of Observational Sciences, Manora Peak, Nainital, Uttarakhand, India, 263129*
[8]*ASI Science Data Center, via Galileo Galilei, I-00044, Frascati, Italy*
[9]*Faculty of Mathematics and Physics, University of Ljubljana, Jadranska 19, SI-1000 Ljubljana, Slovenia*
[10]*Centre of Excellence SPACE-SI, Aškerčeva cesta 12, SI-1000 Ljubljana, Slovenia*
[11]*Dark Cosmology Centre, Niels Bohr Institute, University of Copenhagen, Juliane Maries vej 30, DK-2100 København Ø, Denmark*
[12]*Department of Physics and Astronomy, University of Leicester, University Road, Leicester LE1 7RH, UK*

Accepted 2013 November 17. Received 2013 October 23; in original form 2013 August 10

ABSTRACT

We use high-quality, multiband observations of *Swift* GRB 120404A, from γ-ray to radio frequencies, together with the new hydrodynamics code of van Eerten et al. to test the standard synchrotron shock model. The evolution of the radio and optical afterglow, with its prominent optical rebrightening at $t_{\rm rest} \sim 260$–2600 s, is remarkably well modelled by a decelerating jet viewed close to the jet edge, combined with some early re-energization of the shock. We thus constrain the geometry of the jet with half-opening and viewing angles of 23° and 21°, respectively, and suggest that wide jets viewed off-axis are more common in GRBs than previously thought. We also derive the fireball microphysics parameters $\epsilon_B = 2.4 \times 10^{-4}$ and $\epsilon_e = 9.3 \times 10^{-2}$ and a circumburst density of $n = 240\,{\rm cm}^{-3}$. The ability to self-consistently model the microphysics parameters and jet geometry in this way offers an alternative to trying to identify elusive canonical jet breaks at late times. The mismatch between the observed and model-predicted X-ray fluxes is explained by the *local* rather than the global cooling approximation in the synchrotron radiation model, constraining the microphysics of particle acceleration taking place in a relativistic shock and, in turn, emphasizing the need for a more realistic treatment of cooling in future developments of theoretical models. Finally, our interpretation of the optical peak as due to the passage of the forward shock synchrotron frequency highlights the importance of high-quality multiband data to prevent some optical peaks from being erroneously attributed to the onset of fireball deceleration.

Key words: radiation mechanisms: non-thermal.

1 INTRODUCTION

The observational picture of the gamma-ray burst (GRB) phenomenon has constantly been evolving during the last 15 years since the discovery of the long-lived afterglow radiation in the aftermath of the prompt high-energy emission (see Gehrels & Mészáros 2012, for a recent review). The knowledge of the GRB host galaxies as well as of the circumburst environment properties has been providing important clues to characterize the stellar progenitors, to identify key factors such as metallicity (e.g. see Fynbo, Malesani & Jakobsson 2012; Savaglio 2012, for recent reviews), especially whenever

⋆E-mail: guidorzi@fe.infn.it

a possible associated supernova component cannot be observed due to distance constraints.

In the *Swift* and *Fermi* era, the phenomenology displayed across the electromagnetic spectrum by GRB afterglows appears to be more complex than predicted in the pre-*Swift* epoch (Melandri et al. 2008). In particular, clear-cut achromatic breaks in the light curves associated with the jet angle have turned out to be unexpectedly rare events (Racusin et al. 2009). Likewise, the unexpected paucity of early optical light curves with evidence for reverse shock (RS) emission (Roming et al. 2006) raised the issue of the magnetic energy density entrained in the ejecta as a possible explanation (Zhang & Kobayashi 2005) in addition to other alternatives (e.g. Jin & Fan 2007; Mundell et al. 2007; Melandri et al. 2010; Guidorzi et al. 2011).

Although in many cases fitting full data sets into a self-consistent description of the afterglow evolution proved very problematic (e.g. Covino et al. 2010; Gendre et al. 2010), overall the afterglow emission can be accounted for as synchrotron with possible inverse Compton contributions by the electrons shocked by the GRB blast wave (e.g. Mészáros 2006), with occasional energy injection (e.g. Rossi et al. 2011) and/or the combination of geometric effects (e.g. Guidorzi et al. 2009; Krühler et al. 2009; Margutti et al. 2010).

In this paper, we provide a self-consistent picture of the broad-band data set we collected on GRB 120404A, spanning from radio to X-rays, within the first few days after the GRB itself. To this aim, we fitted the entire data set using the hydrodynamical code recently developed by van Eerten, van der Horst & MacFadyen (2012), which models the synchrotron emission from a relativistic fireball sweeping up homogeneous interstellar medium (ISM) within a uniform conical structure jet with sharp edge. The excellent quality of our data set, combined with the observed complex behaviour, represents a rigorous test for the model and offers the opportunity to strictly constrain the energetics, the geometry of the jet and the microphysics parameters of the shocks. This is one of the first cases in which a realistic (i.e. based on realistic hydrodynamical simulations and not purely analytical) model is applied to a broad-band high-quality data set of a GRB. We also present spectroscopic data of the optical afterglow which allowed us to measure its redshift.

Throughout the paper, times are given relative to the GRB trigger time of *Swift*/BAT, which corresponds to 2012 April 4, 12:51:02 UT. The convention $F(\nu, t) \propto \nu^{-\beta} t^{-\alpha}$ is followed, where F is the flux density and the energy index β is related to the photon index by $\Gamma = \beta + 1$. We adopted the standard cosmological model: $H_0 = 71\,\mathrm{km\,s^{-1}\,mpc^{-1}}$, $\Omega_\Lambda = 0.73$, $\Omega_\mathrm{M} = 0.27$ (Spergel et al. 2003).

All of the quoted errors are given at 90 per cent confidence level for one interesting parameter ($\Delta\chi^2 = 2.706$), unless stated otherwise.

2 OBSERVATIONS

GRB 120404A was detected and localized in real time with the *Swift* Burst Alert Telescope (BAT; Barthelmy et al. 2005) instrument (Stratta et al. 2012) with an accuracy of 3 arcmin. The γ-ray prompt emission in the 15–150 keV energy band lasted about 50 s. A quick-look analysis gave a peak flux of (1.2 ± 0.2) ph $\mathrm{cm^{-2}\,s^{-1}}$, a fluence of about 10^{-6} erg $\mathrm{cm^{-2}}$, and burst coordinates $\alpha(\mathrm{J2000}) = 15^\mathrm{h}40^\mathrm{m}00\overset{\mathrm{s}}{.}4$, $\delta(\mathrm{J2000}) = +12^\circ52'57''$ with an error radius of 1.2 arcmin (Ukwatta et al. 2012).

The *Swift* X-Ray Telescope (XRT; Burrows et al. 2005) began observing at 130 s and promptly found a bright, uncatalogued X-ray source within the BAT error circle. The X-ray source position was later refined using the XRT–Ultraviolet/Optical Telescope (UVOT) alignment and matching UVOT field sources to the USNO-B1 catalogue, with burst coordinates $\alpha(\mathrm{J2000}) = 15^\mathrm{h}40^\mathrm{m}02\overset{\mathrm{s}}{.}28$, $\delta(\mathrm{J2000}) = +12^\circ53'04\overset{''}{.}9$ with an error radius of 1.6 arcsec (Osborne et al. 2012).

The *Swift* UVOT (Roming et al. 2005) began observing at 139 s and from a 147-s exposure in the white filter found an optical candidate with magnitude 19.43 ± 0.12 with coordinates $\alpha(\mathrm{J2000}) = 15^\mathrm{h}40^\mathrm{m}02\overset{\mathrm{s}}{.}29$, $\delta(\mathrm{J2000}) = +12^\circ53'06\overset{''}{.}3$ with an error radius of 0.65 arcsec (Breeveld & Stratta 2012; Stratta et al. 2012).

The UVOT optical candidate was soon confirmed independently by the Faulkes Telescope North (FTN), which began observing 4 min after the GRB trigger time (Guidorzi, Melandri & Japelj 2012). We measured the redshift of $z = 2.876$ with Gemini-North about 1 h after the burst upon the identification of several absorption lines (Cucchiara & Tanvir 2012); this value was later confirmed with the X-shooter instrument (Vernet et al. 2011) at the European Southern Observatory Very Large Telescope (VLT), which observed at 16 h post-burst (D'Elia et al. 2012).

The optical afterglow was observed by a number of facilities: the FTN and the Faulkes Telescope South (FTS) jointly monitored it from 4 min to 5.5 h with the $BVRi'$ filters. The optical light curve exhibited a rebrightening which peaked around 40 min post-burst with a magnitude of $R = 16.9$, as also noted by others (Tristram, Fukui & Sako 2012).

We kept monitoring the afterglow with the Gamma-Ray Burst Optical and Near-Infrared Detector (GROND; Greiner et al. 2008), which started simultaneous observations in $g'r'i'z'JHK$ filters at 18.2 h after the burst (Sudilovsky, Rau & Greiner 2012). We also collected data with the 1.04-m telescope at the Aryabhatta Research Institute of observational sciences (ARIES) in Nainital, India, starting from 6.5 h post-GRB with *RI* filters (Kumar, Bhatt & Pandey 2012).

Finally, we discovered the radio counterpart with the Karl G. Jansky Very Large Array (JVLA; Perley et al. 2011) at 22 GHz at 0.75 d at the position $\alpha(\mathrm{J2000}) = 15^\mathrm{h}40^\mathrm{m}02\overset{\mathrm{s}}{.}28$ (±0.01), $\delta(\mathrm{J2000}) = +12^\circ53'06\overset{''}{.}1$ (±0.1) with a flux density of (88 ± 24) μJy (Zauderer, Laskar & Berger 2012).

The Galactic reddening along the direction to the GRB is $E(B-V) = 0.050$ mag (Schlegel, Finkbeiner & Davis 1998). The Galactic extinction in each filter has been estimated through the NASA/IPAC Extragalactic Database extinction calculator.[1] Specifically, the extinction in each filter is derived through the parametrization by Cardelli, Clayton & Mathis (1989): $A_U = 0.27$, $A_B = 0.22$, $A_{g'} = 0.20$, $A_V = 0.16$, $A_{r'} = 0.15$, $A_R = 0.13$, $A_{i'} = 0.11$, $A_I = 0.10$, $A_J = 0.04$, $A_H = 0.03$ and $A_K = 0.02$ mag.

3 DATA REDUCTION AND ANALYSIS

3.1 Gamma-ray data

We processed the *Swift*/BAT data of GRB 120404A using the latest version of the HEASOFT package (v6.12). We extracted the mask-tagged light curve and energy spectra in the 15–150 keV energy band by adopting the ground refined coordinates provided by the BAT team (Ukwatta et al. 2012). The BAT detector quality map was obtained by processing the closest-in-time enable/disable detector map. Energy calibration was applied using the closest-in-time gain/offset file with the tool BATMASKWTEVT.

[1] http://nedwww.ipac.caltech.edu/forms/calculator.html.

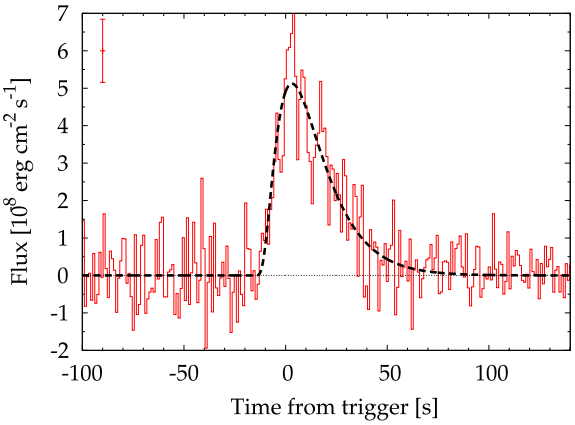

Figure 1. *Swift*/BAT light curve in the 15–150 keV energy band. The dashed line shows the best-fitting model as obtained with the model by Norris et al. (2005). The typical error bar is shown in the upper-left corner.

Fig. 1 shows the mask-weighted 15–150 keV time profile of GRB 120404A recorded by the *Swift*/BAT detector. It consists of a single fast-rise exponential-decay (FRED) pulse peaking at 3 s with a $T_{90} = 48 \pm 16$ s, from −15.5 to 32.5 s. The flux shown is derived assuming the rate-to-flux conversion obtained from the time-integrated spectrum over the T_{90} interval (see below). Fitting the time profile with the model by Norris et al. (2005) gives a satisfactory result (χ^2/d.o.f. = 171/143), as shown by the dashed line in Fig. 1. The parameters used are the peak time $t_{\rm peak}$, the peak flux A, the rise and decay times $\tau_{\rm r}$ and $\tau_{\rm d}$, the pulse width w and the asymmetry k. Their best-fitting values are reported in Table 1. The shape of the pulse with a corresponding decay-to-rise ratio of 2.2 is very typical of classical FREDs (Norris et al. 1996).

The 15–150 keV peak flux is calculated from the spectrum integrated around the peak, from 2.2 to 4.3 s; this can be fitted with a power law with a photon index of 1.9 ± 0.3 (χ^2/d.o.f. = 6.5/8) with a peak flux of $(7.3 \pm 1.2) \times 10^{-8}$ erg cm^{-2} s^{-1} and a peak photon flux of (1.1 ± 0.2) ph cm^{-2} s^{-1}. The 15–150 keV time-integrated spectrum over the T_{90} interval can be fitted with a power law with a photon index of $\Gamma_\gamma = 1.91 \pm 0.15$ and a total fluence of $(1.63 \pm 0.14) \times 10^{-6}$ erg cm^{-2}. Compared with the catalogue of BAT (Sakamoto et al. 2011), GRB 120404A is a medium burst in terms of both peak flux and fluence. The typical low-energy and high-energy photon indices of GRB prompt emission spectra (e.g. Kaneko et al. 2006; Sakamoto et al. 2011) suggest that the peak energy, $E_{\rm p}$, is likely to lie either within or below the 15–150 keV energy band.

Despite the unknown value of $E_{\rm p}$, we can constrain it from the photon index measured with BAT through the relation by Sakamoto et al. (2009) taking into account its large dispersion. We infer that $E_{\rm p}$ is likely to range between ∼1 and 100 keV, corresponding to an intrinsic (i.e. source rest frame) value for $E_{\rm p,\,i}$ between ∼4 and ∼400 keV. We can make a further step by constraining the isotropic-equivalent radiated energy $E_{\gamma,\,\rm iso}$ in the GRB rest-frame 1–10^4 keV energy band. We assume the spectrum to be described with the Band function with typical values for the photon indices, $\alpha_{\rm B} = -1$ and $\beta_{\rm B} = -2.3$ (Kaneko et al. 2006). By propagating the uncertainty on $E_{\rm p}$ in calculating the corresponding $E_{\gamma,\,\rm iso}$, we end up with an estimate of $E_{\gamma,\,\rm iso} = (9 \pm 4) \times 10^{52}$ erg.

We calculated a 3σ upper limit to the average 15–150 keV flux in the time interval from 200 to 800 s. This is roughly simultaneous with a constant optical flux phase preceding the major rebrightening and, as such, is useful to constrain the spectral index of a possible long-lived, low-level prompt emission with an optical counterpart. We obtained an upper limit on the average flux of 6.8×10^{-10} erg cm^{-2} s^{-1}, or, equivalently, $f_{\nu,\,\gamma} < 2.2$ μJy at $\nu_\gamma = 1.2 \times 10^{19}$ Hz (50 keV). Combined with the dust-corrected value for the R band measured during the early constant phase, $f_{\nu,\,R} = 270$ μJy at $\nu_R = 4.7 \times 10^{14}$ Hz, it turns into a lower limit to the average optical-to-γ spectral index, $\beta_{{\rm opt}-\gamma} > 0.5$. The observed $\beta_{{\rm opt}-\gamma}$ distribution for a large number of GRBs is consistent with values larger than 0.5 (Yost et al. 2007a; Kopač et al. 2013), unless one considers GRBs classified as dark (Yost et al. 2007b), most of which are dust extinguished (Fynbo et al. 2009; Perley et al. 2009; Greiner et al. 2011; Zauderer et al. 2013). Hence, the possibility of a long-lasting γ-ray emission below the BAT sensitivity sharing a common origin with the early ($t < 800$ s) optical detection is not at odds with what is observed for most unextinguished GRBs with measured optical and high-energy prompt emission.

3.2 X-ray data

The *Swift*/XRT began observing GRB 120404A on 2012 April 04 at 12:53:25 UT, about 143 s after the trigger, and ended on 2012 April 07 at 22:39:57, with total net exposures of 117 s in window timing and 26.2 ks in photon counting modes spread over 6.9 d. The XRT data were processed following the procedure described in Margutti et al. (2013), applying calibration and standard filtering and screening criteria. The XRT analysis was performed in the 0.3–10 keV energy band.

We extracted the 0.3–10 keV energy spectrum in the time interval from 10.4 to 21.1 ks; later observations did not allow us to collect enough photons to ensure the extraction of another meaningful spectrum. Source and background spectra were extracted from the same regions as those used for the light curve. Spectral channels were grouped so as to have at least 20 counts per bin. The ancillary response files were generated using the task XRTMKARF. Spectral fitting was performed with XSPEC (v. 12.5). The spectrum can be modelled with an absorbed power law with the combination of XSPEC models WABS ZWABS POW, based on the photoelectric cross-section by Morrison & McCammon (1983). The Galactic neutral hydrogen column density along the GRB direction was fixed to the value determined from 21 cm line radio surveys: $N_{\rm H\,I}^{\rm Gal} = 3.4 \times 10^{20}$ cm^{-2} (Kalberla et al. 2005). The additional X-ray absorption, modelled in the GRB rest frame, was found to be $N_{{\rm H\,I},z} = 6.3^{+6.4}_{-5.4} \times 10^{21}$ cm^{-2}, very typical of X-ray afterglow spectra (e.g. Campana

Table 1. Best-fitting parameters of the time profile of the prompt γ-ray pulse as seen in the 15–150 keV band.

$t_{\rm peak}$ (s)	Peak flux (10^{-8} erg cm^{-2} s^{-1})	$\tau_{\rm r}$ (s)	$\tau_{\rm d}$ (s)	w (s)	k	χ^2/d.o.f.
3.1 ± 7.1	5.1 ± 0.3	11.0 ± 2.6	24.3 ± 4.2	35.2 ± 6.6	0.38 ± 0.05	171/143

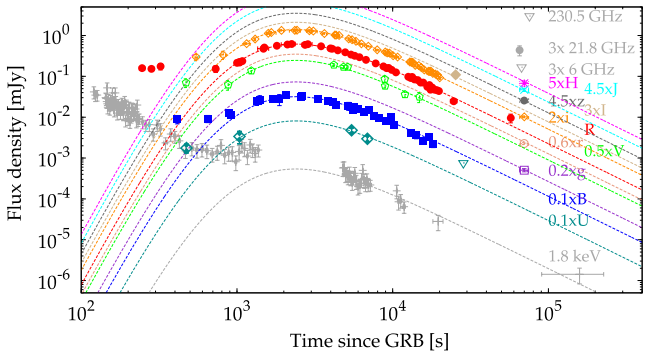

Figure 2. Panchromatic light curve from radio to X-rays of the early afterglow of GRB 120404A. Upside down triangles show upper limits. Normalizations have been rescaled for the sake of clarity. Lines show the result of a simultaneous, achromatic fit of the rebrightening. See the text for further details.

et al. 2012). The X-ray photon index in the 0.3–10 keV energy band is $\Gamma_X = 2.3 \pm 0.3$.

The X-ray unabsorbed flux light curve was derived from the rate curve by assuming the same counts-to-energy factor (5.4×10^{-11} erg cm^{-2} count^{-1}) obtained from the spectrum described above. This implicitly relies on the lack of strong spectral evolution from ∼10 ks onward; although such an assumption cannot be proven due to the paucity of photons at late times, this is in agreement with what is observed for most GRBs (e.g. Evans et al. 2009). Finally, the flux-density curve shown in Fig. 2 was calculated at 1.8 keV, the energy at which the energy spectrum with $\beta_X = \Gamma_X - 1 = 1.3$ has the same value as that averaged over the 0.3–10 keV range. The X-ray light curve can be modelled (χ^2/d.o.f. = 61/100) with a double broken power law with power-law indices $\alpha_1 = 2.28 \pm 0.24$, $\alpha_2 = -0.1 \pm 0.7$, $\alpha_3 = 1.8 \pm 0.3$, and break times $t_1 = (540 \pm 120)$ s, $t_2 = (2480 \pm 460)$ s, respectively, in agreement with previous reports (Stratta et al. 2012).

3.3 Optical and infrared data

Both FTN and FTS carried out robotically triggered observations: FTN observed from 4 to 75 min, while FTS observed from 17 min to 5.6 h. The automatic identification of the afterglow by the GRB pipeline LT–TRAP (Guidorzi et al. 2006) triggered the multifilter ($BVRi'$) observation sequence. The optical afterglow position is $\alpha(\mathrm{J2000}) = 15^{\mathrm{h}}40^{\mathrm{m}}02\overset{\mathrm{s}}{.}30$, $\delta(\mathrm{J2000}) = +12^{\circ}53'06\overset{''}{.}4$ with an error radius of 0.5 arcsec, consistent with the position determined by *Swift*/UVOT (Stratta et al. 2012) and radio observations (Zauderer et al. 2012).

Later observations were carried out with the 1.04-m ARIES telescope with the *RI* filters. Observations started at 6.5 h and last about 1 h through a sequence of four (three) individual frames in the *R* (*I*) filter 300-s exposure each. The afterglow is clearly detected in the co-added frames for both filters.

We observed GRB 120404A with the VLT/X-shooter spectrograph at 15.9 h (D'Elia et al. 2012). In particular, we obtained a photometric estimate in the *R* band from the 30-s exposure acquisition frame.

GROND observed GRB 120404A from 18.2 to 20.7 h simultaneously with the $g'r'i'z'JHK$ filters. The afterglow was clearly detected in all filters, except for *K* for which an upper limit of 20.5 mag was given.

Calibration of the $g'r'i'z'$ frames was performed against five field stars of the Sloan Digital Sky Survey (SDSS; release 6). Magnitudes in the Johnson–Cousins *BVRI* filters for the same calibrating stars were derived from the SDSS values using the transformations by Jordi, Grebel & Ammon (2006). For each filter the scatter in the zero-point was added in quadrature to the statistical uncertainty of each individual frame. Both aperture and point spread function photometry was systematically carried out using the Starlink GAIA software,[2] making sure that both gave consistent results within the uncertainties. In the case of VLT/X-shooter frames, the night was not photometric and we could only use two faint field stars different from the five stars mentioned above; for the acquisition frame, the zero-point was poorly determined with an uncertainty of 0.3 mag. GROND *JHK* filters were first calibrated against nearby 2MASS catalogue stars and then converted to *AB* magnitudes.

Magnitudes were finally converted into flux densities (μJy) following Fukugita, Shimasaku & Ichikawa (1995) and Fukugita et al. (1996). Table 2 reports the photometric set for all near-infrared (NIR)/optical data we collected. Magnitudes are corrected for airmass, while flux densities are also corrected for Galactic reddening.

3.3.1 *Spectroscopy*

On April 4.57 UT we observed the optical afterglow of GRB 120404A with the Gemini-North telescope and the Gemini Multi-Object Spectrograph (GMOS) camera (Hook et al. 2004): we obtained 2 × 900 s spectra, using the B600 grism with the 1 arcsec slit (resolution of about 3.5 Å) centred at 6500 Å, covering wavelengths 5000–8000 Å. The data were analysed using the standard GEMINI/GMOS data analysis packages within the IRAF[3] environment. We performed flat-fielding, wavelength calibration (using a CuAr lamp spectra obtained immediately after the science frames), and cosmic ray rejection using the LACOS_SPEC package (van Dokkum 2001). A sky region close in the spatial direction, but unaffected by the spectral trace, was used for sky subtraction. The two-dimensional spectra were then co-added.

Fig. 3 presents the final co-added spectrum, normalized to the continuum: the afterglow spectrum presents a very complex series of absorption features. The main one, indicated in blue, is associated with the GRB host galaxy (at $z = 2.8767$) thanks to the identification of low- and high-ionized species as well as fine-structure transitions due to the UV radiation of the GRB interacting with the ISM (Prochaska, Chen & Bloom 2006; Vreeswijk et al. 2007). In addition, we were able to identify an unusual set of intervening systems, based on Mg II and C IV doublets identifications, indicating a very complex line of sight (see also, GRB 060418; Vreeswijk et al. 2007). These systems, at $z = 2.551$, 1.776, 1.633, 1.101 and 1.023 are likely associated with galaxies along the lines of sight.

3.4 Radio and mm data

We observed the position of GRB 120404A with the JVLA (Perley et al. 2011) at 21.8 GHz (*K* band) and 6.0 GHz (*C* band) beginning 2012 April 5 at 06:14:39 UT and with the Smithsonian Astrophysical Observatory's Submillimeter Array (SMA; Ho, Moran & Lo 2004) at 230.5 GHz (1.3 mm) beginning 2012 April 5 at 7:27:31 UT. Observations are summarized in Table 3. A source of radio emission

[2] http://starlink.jach.hawaii.edu/starlink.

[3] IRAF is distributed by the National Optical Astronomy Observatory, which is operated by the Association for Research in Astronomy, Inc., under cooperative agreement with the National Science Foundation.

Table 2. Photometric data set of the NIR/optical afterglow of GRB 120404A.

Time[a] (s)	Telescope	Exp. (s)	Filter	Magnitude[b]	Flux[c] (μJy)	Time[a] (s)	Telescope	Exp. (s)	Filter	Magnitude[b]	Flux[c] (μJy)
70023	GROND	4592	K^d	>20.5	<23.3	9134	FTS	30	R	18.36 ± 0.08	157.6 ± 11.2
70023	GROND	4592	H^d	21.1 ± 0.2	13.5 ± 2.3	9428	FTS	60	R	18.34 ± 0.06	160.5 ± 8.6
70023	GROND	4592	J^d	21.4 ± 0.1	10.4 ± 0.9	9873	FTS	120	R	18.46 ± 0.05	143.7 ± 6.5
70023	GROND	4592	z'	22.09 ± 0.06	5.7 ± 3.1	10512	FTS	180	R	18.61 ± 0.05	125.2 ± 5.6
25370	ARIES	900	I	19.71 ± 0.17	36.4 ± 5.3	12619	FTS	30	R	18.88 ± 0.11	97.6 ± 9.4
547	FTN	10	i'	18.58 ± 0.20	148.6 ± 25.0	13072	FTS	30	R	18.96 ± 0.11	90.7 ± 8.7
816	FTN	30	i'	18.45 ± 0.28	167.5 ± 38.1	13352	FTS	60	R	18.89 ± 0.09	96.7 ± 7.7
1154	FTN	60	i'	17.76 ± 0.05	316.2 ± 14.2	13780	FTS	120	R	19.04 ± 0.07	84.2 ± 5.3
1308	FTS	10	i'	17.48 ± 0.08	409.3 ± 29.1	14469	FTS	180	R	19.09 ± 0.05	80.4 ± 3.6
1589	FTS	30	i'	17.13 ± 0.05	565.0 ± 25.4	15092	FTS	120	R	19.23 ± 0.08	70.7 ± 5.0
1662	FTN	120	i'	17.08 ± 0.07	591.6 ± 36.9	15724	FTS	180	R	19.24 ± 0.07	70.1 ± 4.4
1932	FTS	60	i'	16.95 ± 0.04	666.8 ± 24.1	16689	FTS	30	R	19.50 ± 0.15	55.1 ± 7.1
2352	FTN	180	i'	16.95 ± 0.05	666.8 ± 30.0	17177	FTS	30	R	19.38 ± 0.15	61.6 ± 7.9
2432	FTS	120	i'	16.94 ± 0.05	673.0 ± 30.3	17480	FTS	60	R	19.66 ± 0.19	47.6 ± 7.6
2918	FTN	120	i'	16.97 ± 0.06	654.7 ± 35.2	17919	FTS	120	R	19.54 ± 0.08	53.1 ± 3.8
3093	FTS	180	i'	16.99 ± 0.04	642.7 ± 23.2	18549	FTS	180	R	19.66 ± 0.07	47.6 ± 3.0
3643	FTS	120	i'	17.14 ± 0.04	559.8 ± 20.2	19181	FTS	120	R	19.70 ± 0.07	45.9 ± 2.9
4256	FTN	10	i'	17.23 ± 0.06	515.3 ± 27.7	19824	FTS	180	R	19.76 ± 0.05	43.4 ± 2.0
4331	FTS	180	i'	17.24 ± 0.03	510.5 ± 13.9	24668	ARIES	1200	R	20.37 ± 0.15	24.7 ± 3.2
4526	FTN	30	i'	17.26 ± 0.05	501.2 ± 22.6	57288	VLT/XS	30	R	21.4 ± 0.3	9.6 ± 2.3
5219	FTS	10	i'	17.47 ± 0.07	413.1 ± 25.8	70023	GROND	4592	r'	22.61 ± 0.06	3.8 ± 0.2
5484	FTS	30	i'	17.52 ± 0.05	394.5 ± 17.8	471	FTN	10	V	18.70 ± 0.30	139.9 ± 33.8
5810	FTS	60	i'	17.62 ± 0.05	359.8 ± 16.2	878	UVOT	400	V	18.83 ± 0.33	124.1 ± 32.5
6294	FTS	120	i'	17.77 ± 0.04	313.3 ± 11.3	1237	FTS	10	V	17.97 ± 0.16	274.1 ± 37.6
6970	FTS	180	i'	17.92 ± 0.04	272.9 ± 9.9	4191	FTN	10	V	17.61 ± 0.09	381.9 ± 30.4
7956	FTS	120	i'	18.14 ± 0.04	222.9 ± 8.1	4832	UVOT	200	V	17.74 ± 0.10	338.8 ± 29.8
8957	FTS	10	i'	18.27 ± 0.10	197.7 ± 17.4	5144	FTS	10	V	17.74 ± 0.12	338.8 ± 35.4
9219	FTS	30	i'	18.33 ± 0.08	187.1 ± 13.3	8892	FTS	10	V	18.48 ± 0.21	171.4 ± 30.1
9552	FTS	60	i'	18.34 ± 0.05	185.4 ± 8.3	8941	UVOT	5545	V	18.90 ± 0.13	116.4 ± 13.1
10061	FTS	120	i'	18.50 ± 0.05	160.0 ± 7.2	11992	UVOT	550	V	19.42 ± 0.18	72.1 ± 11.0
10754	FTS	180	i'	18.58 ± 0.05	148.6 ± 6.7	14858	FTS	20	V	19.57 ± 0.35	62.8 ± 17.3
12889	FTS	10	i'	18.88 ± 0.15	112.7 ± 14.5	70023	GROND	4592	g'	23.1 ± 0.1	2.5 ± 0.2
13151	FTS	30	i'	18.90 ± 0.09	110.7 ± 8.8	413	FTN	10	B	19.43 ± 0.27	87.8 ± 19.3
13473	FTS	60	i'	18.91 ± 0.08	109.7 ± 7.8	649	FTN	30	B	19.38 ± 0.24	91.9 ± 18.2
13967	FTS	120	i'	19.09 ± 0.06	92.9 ± 5.0	891	UVOT	572	B	19.05 ± 0.20	124.6 ± 21.0
14710	FTS	180	i'	19.10 ± 0.05	92.1 ± 4.1	922	FTN	60	B	19.16 ± 0.12	112.6 ± 11.8
15276	FTS	120	i'	19.23 ± 0.07	81.7 ± 5.1	1340	UVOT	20	B	18.32 ± 0.25	244.0 ± 50.2
15967	FTS	180	i'	19.37 ± 0.05	71.8 ± 3.2	1402	FTS	30	B	18.21 ± 0.30	270.0 ± 65.2
16971	FTS	10	i'	19.45 ± 0.17	66.7 ± 9.7	1691	FTS	60	B	18.16 ± 0.13	282.8 ± 31.9
17256	FTS	30	i'	19.46 ± 0.13	66.1 ± 7.5	1874	FTN	180	B	18.19 ± 0.39	275.0 ± 83.0
17598	FTS	60	i'	19.44 ± 0.12	67.3 ± 7.0	2080	FTS	120	B	17.95 ± 0.08	343.1 ± 24.4
18108	FTS	120	i'	19.58 ± 0.07	59.2 ± 3.7	2567	FTN	120	B	18.05 ± 0.11	312.9 ± 30.1
18796	FTS	180	i'	19.62 ± 0.07	57.0 ± 3.6	2628	FTS	180	B	18.00 ± 0.07	327.6 ± 20.5
19379	FTS	120	i'	19.67 ± 0.07	54.5 ± 3.4	3297	FTS	120	B	18.16 ± 0.10	282.8 ± 24.9
20053	FTS	180	i'	19.85 ± 0.06	46.1 ± 2.5	3858	FTS	180	B	18.28 ± 0.08	253.2 ± 18.0
70023	GROND	4592	i'	22.24 ± 0.06	5.1 ± 2.7	4131	FTN	10	B	18.38 ± 0.11	230.9 ± 22.2
246	FTN	10	R	18.36 ± 0.13	157.6 ± 17.8	4354	FTN	30	B	18.52 ± 0.08	203.0 ± 14.4
283	FTN	10	R	18.40 ± 0.16	151.9 ± 20.8	5200	FTS	40	B	18.60 ± 0.27	188.5 ± 41.5
323	FTN	10	R	18.25 ± 0.21	174.4 ± 30.7	5582	FTS	60	B	18.87 ± 0.18	147.0 ± 22.5
730	FTN	30	R	18.39 ± 0.23	153.3 ± 29.3	5652	UVOT	200	B	18.65 ± 0.10	180.1 ± 15.8
1001	FTS	10	R	18.03 ± 0.13	213.5 ± 24.1	5954	FTS	120	B	18.78 ± 0.11	159.7 ± 15.4
1036	FTN	60	R	17.97 ± 0.07	225.7 ± 14.1	6509	FTS	180	B	18.98 ± 0.11	132.9 ± 12.8
1041	FTS	10	R	18.01 ± 0.13	217.5 ± 24.5	7088	UVOT	200	B	18.86 ± 0.12	148.4 ± 15.5
1082	FTS	10	R	17.92 ± 0.15	236.3 ± 30.5	7605	FTS	120	B	19.21 ± 0.15	107.5 ± 13.9
1479	FTN	120	R	17.16 ± 0.09	475.8 ± 37.9	8173	FTS	180	B	19.31 ± 0.12	98.0 ± 10.3
1500	FTS	30	R	17.09 ± 0.05	507.5 ± 22.8	9088	FTS	100	B	19.52 ± 0.20	80.8 ± 13.6
1806	FTS	60	R	16.98 ± 0.06	561.7 ± 30.2	9699	FTS	120	B	19.28 ± 0.17	100.8 ± 14.6
2106	FTN	180	R	16.90 ± 0.03	604.6 ± 16.5	10266	FTS	180	B	19.76 ± 0.16	64.8 ± 8.9
2249	FTS	120	R	16.87 ± 0.03	621.5 ± 16.9	13208	FTS	220	B	20.24 ± 0.20	41.6 ± 7.0
2735	FTN	120	R	16.92 ± 0.08	593.6 ± 42.2	14166	FTS	180	B	20.39 ± 0.22	36.3 ± 6.7
2857	FTS	180	R	16.89 ± 0.03	610.2 ± 16.6	15611	FTS	540	B	20.75 ± 0.20	26.0 ± 4.4
3470	FTS	120	R	17.02 ± 0.03	541.3 ± 14.8	17113	UVOT	907	B	20.51 ± 0.16	32.5 ± 4.4
3989	FTN	30	R	17.15 ± 0.04	480.3 ± 17.4	18243	FTS	700	B	20.95 ± 0.20	21.6 ± 3.6

Table 2 – *continued*

Time[a] (s)	Telescope	Exp. (s)	Filter	Magnitude[b]	Flux[c] (μJy)	Time[a] (s)	Telescope	Exp. (s)	Filter	Magnitude[b]	Flux[c] (μJy)
4090	FTS	180	*R*	17.16 ± 0.03	475.8 ± 13.0	474	UVOT	246	*U*	20.06 ± 0.26	17.6 ± 4.2
4436	FTN	30	*R*	17.26 ± 0.04	434.0 ± 15.7	1039	UVOT	58	*U*	19.35 ± 0.36	33.7 ± 11.3
4950	FTS	30	*R*	17.38 ± 0.05	388.6 ± 17.5	5447	UVOT	197	*U*	18.97 ± 0.15	47.9 ± 6.4
5398	FTS	30	*R*	17.52 ± 0.05	341.6 ± 15.4	6883	UVOT	197	*U*	19.49 ± 0.20	29.6 ± 5.6
5698	FTS	60	*R*	17.60 ± 0.05	317.3 ± 14.3	28449	UVOT	396	*U*	> 21.0	< 7.6
6121	FTS	120	*R*	17.69 ± 0.04	292.1 ± 10.6	104796	UVOT	1678	*U*	> 21.8	< 3.4
6738	FTS	180	*R*	17.84 ± 0.04	254.4 ± 9.2	173817	UVOT	1687	*U*	> 21.8	< 3.4
7780	FTS	120	*R*	18.06 ± 0.05	207.7 ± 9.3	256985	UVOT	1687	*U*	> 21.8	< 3.4
8717	FTS	30	*R*	18.24 ± 0.07	176.0 ± 11.0						

Note. Uncertainties are 1σ.
[a]Mid-point time from the GRB onset time.
[b]Corrected for airmass.
[c]Corrected for Galactic extinction.
[d]*AB* magnitudes.

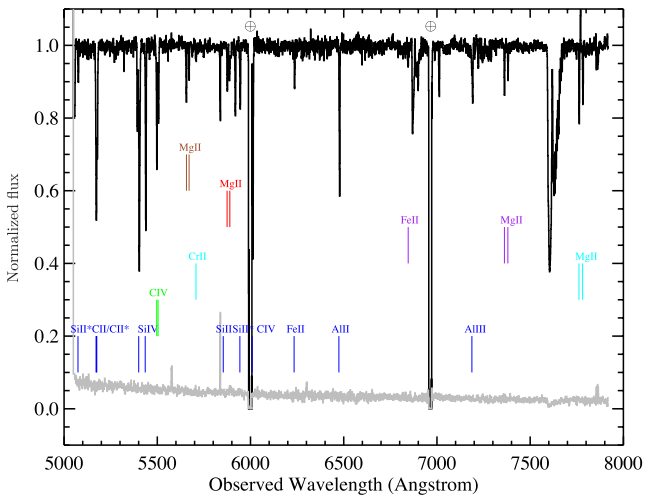

Figure 3. Continuum normalized spectrum of GRB 120404A observed with the Gemini-North (black is the spectrum and grey is the error array associated with it): the main system at $z = 2.8767$ (blue) is associated with the GRB host galaxy and presents several low- and high-ionized species as well as fine-structure transitions features (e.g. S II*, C II, C II*, Si IV, C IV). In addition, four more systems have been identified, based on the identification of metal lines: $z = 2.551$ (green, C IV), $z = 1.776$ (cyan, Cr II, Mg II doublet), $z = 1.633$ (purple, Fe II and Mg II), $z = 1.101$ (red, Mg II) and $z = 1.023$ (brown, Mg II).

was detected at 21.8 GHz with a flux of 87.6 ± 24.0 μJy at a position of $\alpha = 15{:}40{:}02.28$ ($\pm$ 0.01) and $\delta = 12{:}53{:}06.1$ ($\pm$0.1), with 1σ positional uncertainties. This radio position is consistent with both the *Swift*/XRT position (Osborne et al. 2012) and the UVOT position (Stratta et al. 2012). No significant source of emission was detected at the position of GRB 120404A at 6.0 GHz with the VLA to a 3σ upper limit of 33.6 μJy or at 230.5 GHz with the SMA to a 3σ upper limit of ∼3 mJy.

VLA observations utilized the Wideband Interferometric Digital ARchitecture (WIDAR) correlator (Dougherty & Perley 2010), with 1.024 GHz bandwidth in each of the upper and lower sidebands (eight intermediate frequencies per sideband, each with 64, 2 mHz channels). At the *K* band, we centred the frequency for each sideband at 19.1 and 24.4 GHz, with a mean frequency of 21.8 GHz. At the *C* band, we centred the frequency for each sideband at 4.9 and 7.0 GHz, with a mean frequency of 6.0 GHz. In practice, after flagging edge channels and excising Radio Frequency Interference (RFI), we obtained a total continuum bandwidth of ∼75−85 per cent (at the *C* band where there is more RFI and the *K* band, respectively).

For VLA observations, we calibrated our bandpass and flux scaling using 3C286, and performed gain calibrations with J1553+1256 (3.°3 from GRB 120404A). Observations were obtained in the C configuration (maximum baseline ∼3.4 km), and the synthesized beam size is noted in Table 3. Reference pointing offsets were measured and applied prior to bandpass/flux observations using 3C286 and prior to the gain calibrator/source observations using J1608+1029 at 8.4 GHz, according to standard VLA procedures. Flagging, calibration and imaging were performed using standard procedures in Astronomical Image Processing System (AIPS; Greisen 2003).

SMA 230.5 GHz observations were obtained in the very extended configuration, with baseline lengths ranging from 103 to 476 m. The synthesized beam size is noted in Table 3. Neptune and Titan were utilized for flux measurements, 3C454.3 and 3C279 for bandpass, and 1550+054 and 1540+147 for gain calibration. Data reduction was performed using standard MIRIDL and MIRIAD procedures.

4 MODELLING AND INTERPRETATION

4.1 Broadband fitting

We modelled the multifilter light curves simultaneously by imposing common power-law indices, given the apparent lack of evidence for strong chromatic evolution during the rebrightening. We adopted the same approach as for past events (e.g. see Guidorzi et al. 2011) with important changes: in the previous treatment, the different normalizations of each filters, initially treated as independent parameters, were then used to construct a spectral energy distribution (SED). In this case, we adopted a more general approach, since we fitted both the temporal and spectral dependence of the flux density at different wavelengths simultaneously. We assumed the SED to be described by a simple power-law model, $F(\nu, t) \propto \nu^{-\beta_0} \times 10^{-0.4\,A(\nu)}$, where the term $A(\nu)$ accounts for the rest-frame dust extinction as modelled according to three different (SMC, LMC, MW) profiles in the Pei (1992) parametrization. The temporal behaviour was modelled in the time interval from 800 to 2×10^5 s, i.e. from the rebrightening onset. The complete model describing the temporal evolution of flux densities at all optical wavelengths is given in

Table 3. Radio data.

Frequency[a] (GHz)	Start time[b] (days)	Int src[c] (min)	rms[d] (μJy/bm)	Integrated flux[e] (μJy)	Beam size[f] (arcsec)	Observatory
21.8*	0.75	17.5	25.3	87.6 ± 24.0	1.1×0.85	VLA
19.1	–	–	31.8	70.6 ± 30.2	1.2×0.94	–
24.4	–	–	39.0	112.7 ± 37.0	0.97×0.77	–
6.0*	0.77	23.3	11.2	<33.6	3.1×2.7	VLA
4.9	–	–	17.2	<51.6	3.8×3.5	–
7.0	–	–	14.0	<42.0	2.7×2.5	–
230.5	0.77	302.5	$\sim 10^3$	$\lesssim 3 \times 10^3$	0.5×0.4	SMA

[a]Mean frequency of observations. The asterisk indicates redundancy, as it is the mean of two sidebands listed below.
[b]Since the GRB.
[c]Integration time on source.
[d]Measured with IMSTAT in AIPS.
[e]Integrated flux using AIPS task JMFIT to fit a Gaussian, fixing size to clean beam.
[f]Synthesized clean beam size. The source for the *K*-band detection is not resolved, so this is just the beam size.

Table 4. Spectral and temporal best-fitting parameters describing the evolution of the flux densities at optical and X-ray wavelengths.

Data	Dust	F_{15}^a (mJy)	β_o	A_V^b (mag)	α_1	t_p (s)	α_2	n	χ^2/d.o.f.
Optical	MW	1.89 ± 0.09	1.05 ± 0.09	0.22 ± 0.05	$-7.5^{+5.2}_{-4.6}$	2395 ± 55	1.89 ± 0.06	$0.16^{+0.16}_{-0.08}$	89/124
Optical	LMC	1.93 ± 0.12	$0.39^{+0.25}_{-0.22}$	0.32 ± 0.08	-6.6 ± 3.7	2400 ± 55	1.86 ± 0.06	$0.19^{+0.15}_{-0.09}$	98/124
Optical	SMC	1.67 ± 0.20	$-0.23^{+0.68}_{-0.37}$	0.32 ± 0.09	-6.4 ± 3.7	2401 ± 55	1.86 ± 0.06	$0.19^{+0.16}_{-0.09}$	125/124
Opt–X	MW	1.89 ± 0.06	1.05 ± 0.03	0.22 ± 0.04	$-7.2^{+4.7}_{-4.3}$	2397 ± 55	1.88 ± 0.06	$0.16^{+0.16}_{-0.08}$	103/150
Opt–X	LMC	1.57 ± 0.05	1.04 ± 0.02	0.12 ± 0.03	$-7.2^{+4.7}_{-4.2}$	2399 ± 55	1.89 ± 0.05	$0.17^{+0.16}_{-0.09}$	172/150
Opt–X	SMC	1.42 ± 0.05	1.04 ± 0.02	0.07 ± 0.02	-7.5 ± 4.5	2397 ± 55	1.90 ± 0.05	$0.16^{+0.16}_{-0.08}$	167/150

[a]Flux density at the rest-frame frequency of 10^{15} Hz, at peak and corrected for dust extinction.
[b]Rest-frame quantity.

equation (1),

$$F(\nu, t) = F_{15}\, \nu_{15}^{-\beta_0}\, 10^{-0.4\, A(\nu)} \left[\frac{1 - \alpha_1/\alpha_2}{\left(\frac{t}{t_p}\right)^{n\alpha_1} + \left(\frac{t}{t_p}\right)^{n\alpha_2} \left(-\frac{\alpha_1}{\alpha_2}\right)} \right]^{1/n}, \quad (1)$$

where the free parameters are F_{15}, i.e. the dust-unextinguished flux density at $\nu = 10^{15}$ Hz ($\nu_{15} = \nu/10^{15}$ Hz) at the peak time ($t = t_p$), the spectral index β_0, the extinction A_V incorporated in the term $A(\nu)$, the rise ($\alpha_1 < 0$) and decay ($\alpha_2 > 0$) power-law indices, the peak time t_p, the smoothness parameter n. Frequencies are expressed in the GRB rest frame. We chose to use the peak time rather than the break time (e.g. see the parameter t_{b1} in equation 1 of Guidorzi et al. 2011), as the free parameter, since t_p is the interesting parameter and its uncertainty does not have to be calculated taking into account the complicated covariance with other free parameters as it is required for derived (i.e. not free) quantities. Best-fitting parameters were found by minimizing the total χ^2, as expressed in equation (2),

$$\chi^2(F_{15}, \beta_0, A_V, \alpha_1, \alpha_2, t_p, n) = \sum_{k,i} \left(\frac{F(\nu_k, t_{k,i}) - F_{\nu_k,i}}{\sigma_{\nu_k,i}} \right)^2, \quad (2)$$

where $F_{\nu_k,i}$ and $\sigma_{\nu_k,i}$ are the measured flux density and uncertainty for $\nu = \nu_k$ at the time $t = t_{k,i}$. The observed filter U has an effective rest-frame wavelength of 890 Å, i.e. bluewards of the Lyman limit of 912 Å. Its flux density is thus heavily suppressed by the neutral hydrogen along the sightline. Because of this, we let the normalization constant for the U filter to be independently determined by the fitting procedure.

The first three lines in Table 4 report the results obtained by fitting the optical data alone with the three different dust extinction profiles. Although all of the extinction profiles yield formally acceptable χ^2 values, in the following we show that only the MW profile provides a plausible and self-consistent description of the SED. All models provide identical temporal evolution of the light curves, the only discrepancies concerning the spectral parameters. As is often the case, the rise slope is determined with large uncertainty, whereas the decay slope is more accurately measured, $\alpha_2 = 1.9 \pm 0.1$. The peak time essentially remains the same, around 2.4 ± 0.6 ks, regardless of the model adopted.

While in Section 4.1.2 we modelled a detailed optical–X-ray SED taking into account the X-ray spectral shape itself, here we preliminarily added the X-ray flux history obtained by assuming a constant count-to-flux conversion. We determined the reference energy $\hat{E} = 1.8$ keV, i.e. the energy at which the flux density is the same as the average one in the XRT passband 0.3–10 keV for a power-law spectrum with $\Gamma_X = 2.3$ obtained in Section 3.2. Excluding the initial steep decay ($t < 800$ s), which clearly has a different origin from the subsequent emission, X-rays exhibit the same temporal behaviour as the optical photons. This justifies a common fit. For the same reason, we also exclude the presence

of any break frequency between optical and X-rays, so a simple power law appears to be the only plausible spectrum. Fitting all data sets together, one obtains almost identical results for the MW extinction profile, which is still the best model by far, as reported in the last three lines of Table 4. For the two remaining profiles, forcing no break between optical and X-rays clearly changes the spectral index from the corresponding previous cases where X-ray data had not been considered. Although these models cannot be rejected solely because of their χ^2 values, the modelling obtained assuming a MW profile offers by far the best, and most self-consistent description of our data, thus lending support to the evidence for the presence of a 2175 Å bump. The resulting MW-profile-based model for each light curve is shown together with data in Fig. 2.

From the accurate spectral and temporal modelling, we can estimate the total energy released in the optical-to-X-ray frequency range during the rebrightening from 800 s on, $E_{\rm reb}$, properly corrected for dust extinction. Strictly speaking, since the low-energy part of the SED as well as the flux at early times ($t < 800$ s) are poorly known, our estimate should be taken as a lower limit. However, taking into account the uncertainty on α_1 and extrapolating the power-law spectrum to much lower frequencies, the result does not change by more than a factor of 2.

$$E_{\rm reb} \gtrsim \frac{4\pi D_{\rm L}^2}{1+z} \int_{\nu_H}^{\nu_{\rm x}} {\rm d}\nu \int_{800\,{\rm s}}^{+\infty} {\rm d}t\ F(\nu,t) 10^{0.4A(\nu)}$$

$$= 15\, F_{15} \left(\frac{\nu_{\rm x,15}^{1-\beta} - \nu_{\rm H,15}^{1-\beta}}{1-\beta} \right) {\rm erg} \ = \ 2 \times 10^{52}\ {\rm erg}, \qquad (3)$$

where $D_{\rm L} = 7.6 \times 10^{28}$ cm is the luminosity distance. Hence, the energy released during the rebrightening is a non-negligible fraction of the isotropic-equivalent one released in the prompt emission, $E_{\gamma,\,\rm iso} = (9 \pm 4) \times 10^{52}$ erg (Section 3.1).

4.1.1 *Evidence for chromaticity*

Although a simple, achromatic model for the rebrightening and subsequent decay was shown to provide an acceptable description, we investigated whether there exists evidence for chromatic evolution, by allowing different peak times for the light curves at different wavelengths. To this aim, we applied the same fitting procedure as in Section 4.1, but allowing independent peak times for the best sampled filters: i', R, V, B and X-ray. For the remaining filters, we used the sample peak time as that of the closest-in-frequency filter among those treated as free parameters. Limiting to the best-fitting case given by the MW dust extinction one, the total χ^2/d.o.f. improved from that obtained in the strictly achromatic case, 103/150, to 89/146. Such values for the total χ^2, being smaller than 1, probably reflect that uncertainties on individual measures have likely been overestimated following a conservative approach. Formally, the p-value according to the additive F-test is 4×10^{-4}. However, the small χ^2 values suggest a more conservative F-test calculation assuming a unitary reduced χ^2 for the chromatic model, which yields a p-value of 1.0 per cent. We therefore conclude that there is evidence for chromatic evolution with $\lesssim$1 per cent confidence. What is more, the peak time as a function of wavelength follows a precise trend: the higher the effective frequency, the earlier the light curve seems to peak, as reported in Table 5. Should the improvement be entirely due to chance, one would expect no such trend between peak time and frequency. Modelling this dependence with a power law, $\nu_{\rm eff} \propto t^{-\delta}$, yields $\delta = 12 \pm 4$, where the time origin was fixed to the GRB trigger time. Interpreting this as the crossing of a given break frequency through different filters at different times, as one would expect for the synchrotron spectrum evolution, the temporal dependence is too strong to match any theoretical expectation, unless one resets the time origin. Ignoring the X-ray band, the same index is poorly constrained, $\delta = 6 \pm 3$, which still implies a strong evolution. Overall, the evidence for a time lag in the peak as a function of frequency cannot be considered compelling, but surely plausible and likely.

Table 5. Peak time as a function of rest-frame frequency.

Observed filter	Rest-frame $\nu_{\rm eff}$ (10^{15} Hz)	Peak time $t_{\rm p}$ (s)
i'	1.56	2420 ± 40
R	1.81	2360 ± 60
V	2.14	2350 ± 140
B	2.67	2220 ± 100
X	1686	1310^{+170}_{-150}

4.1.2 *Optical-to-X-ray spectral energy distribution*

Although XRT could not collect data around the optical peak, still the available data support the view that, after the initial steep decay, the X-ray flux underwent the same temporal rebrightening followed by an analogous power-law decay. We therefore accumulated an X-ray energy spectrum right after the optical peak, from 4.7 to 7.3 ks, i.e. when the final power-law decay with $\alpha_2 = 1.9$ already set in. The reference time when the instantaneous flux is the same as the average one over the above time interval, is found to be $\hat{t} = 5.9$ ks. To determine the optical flux densities at each wavelength, we ran the multifilter procedure of Section 4.1. However, we did not model the spectral parameters, but we introduced an independent normalization term for each light curve to be freely determined, in the same fashion as we used to do for previous GRBs (e.g. Guidorzi et al. 2011). Not surprisingly, the temporal parameters describing the light-curve evolution did not change (Table 4). The best-fitting normalizations at each filter, expressed as flux densities at peak, are reported in Table 6.

Table 6. Best-fitting flux densities at peak.

Parameter	Value	Unit
F_H	1850^{+750}_{-530}	μJy
F_J	1420^{+300}_{-250}	μJy
F_z	778^{+114}_{-100}	μJy
F_I	785^{+260}_{-200}	μJy
F_i	699 ± 16	μJy
F_R	618 ± 13	μJy
F_r	512 ± 8	μJy
F_V	500^{+43}_{-40}	μJy
F_g	344^{+73}_{-61}	μJy
F_B	318 ± 14	μJy
F_U	81^{+19}_{-15}	μJy
χ^2/d.o.f.	83/117	

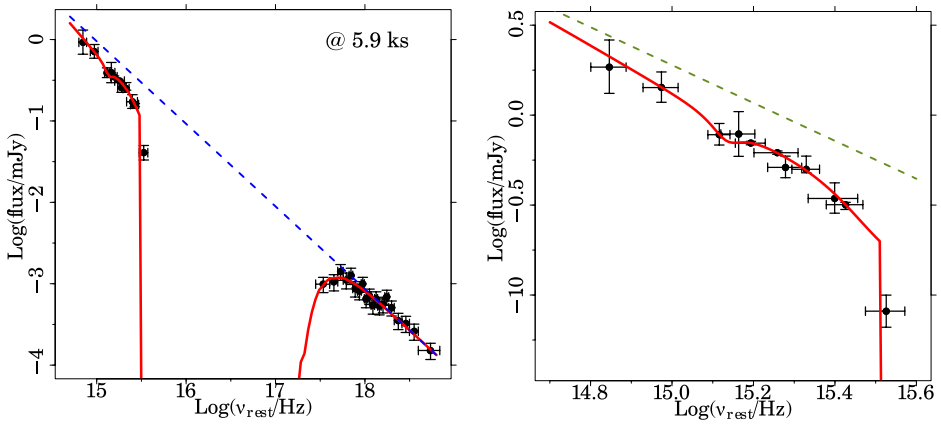

Figure 4. Left-hand panel: rest-frame optical–X SED at $\hat{t} = 5.9$ ks. The solid line shows the best-fitting model obtained with a MW extinction profile and a simple power law with index $\beta = 1.01 \pm 0.03$. The dashed line shows the SED one would have observed in the absence of dust. Right-hand panel: close-in of the optical points.

Optical flux densities at the X-ray spectrum reference time $\hat{t}$ were calculated simply by rescaling the corresponding peak values using the temporal model in Table 4, which yielded a factor of 0.50. We thus constructed an optical–X SED at $\hat{t}$ by rescaling the optical flux densities. Given the same temporal decay exhibited by optical and X-ray profiles, no break frequency in between is to be expected, consistently with the simple power-law model adopted in Section 4.1.

In addition to modelling the dust extinction, we also had to account for the photoelectric absorption which suppressed the soft X-ray flux. We modelled this using the photoelectric cross-section as parametrized by Morrison & McCammon (1983). The amount of gas responsible for this absorption was modelled in terms of neutral hydrogen column density evaluated in the GRB rest frame, $N_{\rm H}$, assuming solar abundances. The Galactic contribution was accounted for separately.

The only acceptable model is that obtained assuming a MW extinction profile. Its best-fitting parameters were: $\beta = 1.01 \pm 0.03$, $A_V = 0.24 \pm 0.07$ mag, $N_{\rm H} = 5.2^{+2.6}_{-1.7} \times 10^{21}$ cm^{-2}, χ^2/d.o.f. $= 32.4/27$, with a null hypothesis probability of 22 per cent (Table 4). This result is fully compatible with what is obtained adopting the same extinction profile when we fitted the optical data alone (Section 4.1). The result is shown in Fig. 4.

4.2 The standard afterglow model

In the context of the standard afterglow model (see, e.g. Mészáros 2006; Gao et al. 2013; van Eerten 2013 for reviews), a population of shock-accelerated electrons cools through synchrotron emission, resulting in spectra and light curves that are characterized by power-law segments, which join at given break frequencies. The electron energy distribution is assumed to be $\mathrm{d}N/\mathrm{d}\gamma \propto \gamma^{-p}$ ($\gamma > \gamma_m$). Typical values for p found from GRB afterglow modelling range between 2 and 3, in broad agreement with theoretical expectations (e.g. Spitkovsky 2008). At sufficiently late times the afterglow emission is dominated by the forward shock (FS), i.e. the emission due to the shocked ISM, because the emission of the RS – which propagates within the ejecta – is short lived. At such times, the corresponding observed spectral and temporal decay indices for GRB 120404A are $\beta = 1.0$ and $\alpha_2 = 1.9$ (Table 4), with no apparent break from optical through X-rays (Fig. 4). Using $\nu_{\rm m,\,f}$ and $\nu_{\rm c,\,f}$ for synchrotron injection and cooling frequencies, respectively, associated with the FS, the most plausible scenario is the slow cooling regime at $\nu_{\rm m,\,f} < \nu_{\rm opt} < \nu_{\rm x} < \nu_{\rm c,\,f}$, for which $\beta = (p-1)/2$ yields $p = 3$. The decay index depends on the density profile of the circumstellar medium density such that for a homogeneous (wind) medium $\alpha = 3(p-1)/4 = 1.5$ ($\alpha = (3p-1)/4 = 2$).

Thus, simple analytical expectations show that a density profile more akin to a wind could be compatible with the observed spectral and temporal afterglow properties at late times. The closer in time to the initial prompt emission, the more complicated is the overall description of the observed radiation, due to multiple overlapping components from co-located or distinct emitting regions: e.g. an emitting RS, energy injection due to on-going activity of the inner engine, or the onset of the afterglow itself due to the deceleration of the ejecta by the surrounding medium.

Large and accurate broad-band data sets for a given GRB afterglow hold the potential to self-consistently constrain the geometry and dynamics of the relativistic outflow, the density profile of the circumstellar medium, as well as the detailed microphysics of the shock acceleration of electrons and local magnetic field generation. Here we show that even at late time, when most of the jet energy has already been transferred to the shocked ambient medium, a realistic and detailed physical description requires comparably realistic modelling. To do this, we adopt the model developed by van Eerten et al. (2012). In addition, we model, separately, the early time emission ($t < 800$ s) when the afterglow is likely to be dominated by RS emission.

4.3 Relativistic shock physics and jet geometry

The interpretation of the late time broad-band rebrightening in terms of radiation coming from an off-axis jet which finally reaches the observer proved successful in a number of similar cases, such as GRB 081028 (Margutti et al. 2010). We investigated the plausibility of this scenario for GRB 120404A by fitting our multifrequency data set with the BOXFIT code.[4] This code assumes a homogeneous jet with sharp edges ploughing into a constant density medium; it is possible to calculate afterglow light curves and spectra due to synchrotron radiation at any observer time and frequency and the code performs data fitting with the downhill simplex method combined with simulated annealing. The blast wave dynamics have been calculated for 19 high-resolution, 2D jet simulations performed with

[4] http://cosmo.nyu.edu/afterglowlibrary/index.html

Table 7. Best-fitting physical parameters obtained from modelling the multi-afterglow data with the BOXFIT code (van Eerten et al. 2012) combined with an early time additional component. Frozen values are in square brackets.

Data set[a]	$F_{\rm r,\,m,\,i}$[b] (mJy)	$t_{\rm r,\,b}$ (s)	s	$E_{\rm iso}$ (10^{53} erg)	θ_0 (°)	$\theta_{\rm obs}/\theta_0$	n (cm^{-3})	p	ϵ_B (10^{-4})	ϵ_e (10^{-2})	ξ_N	χ^2/d.o.f.
(1)	–	–	–	1.8	26	0.96	86	3.6	4.7	8.3	[1.0]	451/162
(2)	–	–	–	$1.9^{+0.7}_{-0.1}$	$23.1^{+0.8}_{-4.1}$	0.93 ± 0.01	240^{+10}_{-90}	3.8 ± 0.1	$2.4^{+0.1}_{-0.3}$	$9.3^{+0.5}_{-3.4}$	0.99	173/122
(3)	$0.37^{+0.22}_{-0.14}$[c]	930 ± 400[c]	$3.0^{+1.5}_{-1.1}$[c]	$1.9^{+0.7}_{-0.1}$	$23.1^{+0.8}_{-4.1}$	0.93 ± 0.01	240^{+10}_{-90}	3.8 ± 0.1	$2.4^{+0.1}_{-0.3}$	$9.3^{+0.5}_{-3.4}$	0.99	176/128
(3)	0.36 ± 0.06[d]	710 ± 200[d]	–	$1.9^{+0.7}_{-0.1}$	$23.1^{+0.8}_{-4.1}$	0.93 ± 0.01	240^{+10}_{-90}	3.8 ± 0.1	$2.4^{+0.1}_{-0.3}$	$9.3^{+0.5}_{-3.4}$	0.99	178/129

[a](1) Radio to X, $t > 800$ s; (2) radio to UV, $t > 800$ s; (3) radio to UV, all.
[b]The normalization is the flux density at the reference time $t_{\rm ref} = 100$ s.
[c]An additional refreshed RS component was adopted, where the i'-band normalization $F_{\rm r,\,m,\,i}$ and end time of energy injection $t_{\rm r,\,b}$ only were left free to vary. We assumed slow cooling for the RS, with $\nu_{\rm m,\,r} < \nu_{\rm opt} < \nu_{\rm c,\,r}$. $M(>\gamma) \propto \gamma^{-s}$ is the ejected mass moving with Lorentz factors greater than γ (Sari & Mészáros 2000).
[d]An additional RS component was adopted, where the normalization $F_{\rm r,\,m,\,i}$ and crossing time of $\nu_{\rm m,\,r}$ through the i' band only were left free to vary. We assumed slow cooling for the RS.

the relativistic adaptive mesh (RAM) parallel relativistic hydrodynamical code. Exploiting the scale invariance of different jets with different energies and circumburst densities, the code calculates spectra and light curves by solving the linear radiative transfer equations including synchrotron self-absorption. At the cost of a relatively limited amount of computational time, it properly accounts for features such as jet decollimation, inhomogeneity along the shock front, and its late transition to non-relativistic regime. The free parameters include the jet geometry, the energetics and circumburst properties, the released energy and the microphysics parameters which determine the basic properties of the synchrotron radiation caused by the relativistic shocks.

We fitted our broad-band data set with the '*Fermi*' hybrid server for high performance computing of the University of Ferrara, equipped with 188 GB DDR3 of RAM memory.[5] The free parameters were the jet half-opening angle θ_0, the isotropic-equivalent total released energy $E_{\rm iso}$, the circumburst number density n, the viewing angle $\theta_{\rm obs}$, the electron energy distribution index p, the fractions of internal energy going into magnetic fields and accelerated electrons, ϵ_B and ϵ_e, respectively, and the fraction of accelerated electrons, ξ_N. The code assumes that the fireball energy has already been transferred to the ISM, since it makes use of the Blandford–McKee solution (Blandford & McKee 1976) as long as the Lorentz factor of the shocked interstellar matter is high enough. Consequently, the free parameters exclusively concern the propagation and the radiation of the FS.[6]

First, we corrected all the optical flux densities for a factor corresponding to how much the flux in each filter had been suppressed due to the local dust, because the code does not account for it. In this case, thanks to the robust estimate we obtained for the dust content (Section 4.1.2), this should not introduce a big source of uncertainty and, in any case, the correction was within a factor of 2 for all cases, except for the U filter. We obtained a remarkably good result for all the radio and optical data points starting from the onset of the rebrightening onwards, i.e. at $t > 800$ s. However, in none of the allowed cases the best-fitting result could provide a successful match of the X-ray data, for which the best-fitting solution underestimates the X-ray flux by more than a factor of 10. The best-fitting parameters obtained in this case are the following (Table 7): $E_{\rm iso,\,53} = 1.8$, $n_0 = 86$, $\theta_0 = 26°$, $\theta_{\rm obs} = 25°$, $p = 3.6$, $\epsilon_{B,-4} = 4.7$, $\epsilon_{e,-2} = 8.3$, with ξ_N fixed to 1.0 (χ^2/d.o.f. $= 451/162$), where $\epsilon_{B,-4} = \epsilon_B/10^{-4}$ and $\epsilon_{e,-2} = \epsilon_e/10^{-2}$.

[5] http://fermi.unife.it
[6] We made sure that results did not depend appreciably on the adopted value for the `BM_start` parameter, by choosing a range of plausible values for it, as recommended by the code's authors.

4.3.1 *X-ray excess and local cooling*

A possible explanation for the underestimated X-ray flux likely lies in the global cooling time approximation, which is known to systematically underestimate the flux beyond the cooling break (van Eerten, Zhang & MacFadyen 2010). The model adopted by the fitting code assumes a common synchrotron cooling time for all the fluid cells which are contributing to the observed spectrum. In reality, electrons are shock accelerated at the blast wave front at different times for different fluid cells. As a result, the cooling time should be calculated from the time at which each local fluid element is shocked, which has a local dependence. The cooling frequency should be calculated with a much higher spatial resolution than the fluid scale. In the global cooling approximation, the plasma is treated as a whole rather than locally. Consequently, the flux above the cooling frequency is systematically underestimated by a factor, which can be of the order of 10 or more, as shown by van Eerten et al. (2010). Indeed, the X-ray flux curve matches the overall observed behaviour and the shift required for a good match can in principle be entirely explained replacing the global cooling with the more realistic local cooling approximation.

Under the assumption that the mismatch between model and X-ray data is accounted for by the global cooling approximation, we ignored X-rays and fitted the remaining data set. The result is shown in Fig. 5 (dashed lines) and corresponds to the following set of best-fitting parameters: $E_{\rm iso,53} = 1.9^{+0.7}_{-0.1}$, $n_0 = 240^{+10}_{-90}$, $\theta_0 = 23.1^{+0.8}_{-4.1}$ degrees, $\theta_{\rm obs} = (0.93 \pm 0.01)\,\theta_0$, $p = 3.8 \pm 0.1$, $\epsilon_{B,-4} = 2.4^{+0.1}_{-0.3}$, $\epsilon_{e,-2} = 9.3^{+0.5}_{-3.4}$, $\xi_N = 1.0_{-0.4}$ (χ^2/d.o.f. $= 173/122$). The parameters' uncertainties were calculated through the Monte Carlo procedure implemented in the code after determining the partial derivatives around the minimum. Although formally the quality of the fit is still poor (null hypothesis probability of 0.2 per cent), the overall capability of the code to reproduce the multiband light curves from radio to UV is noteworthy. In particular, the fit residuals amount to a few per cent for the most accurate data points, whose uncertainties are comparably small.

4.4 The nature of the early optical emission

The early optical emission is likely to be produced by a separate emission process from that of the later time emission given the

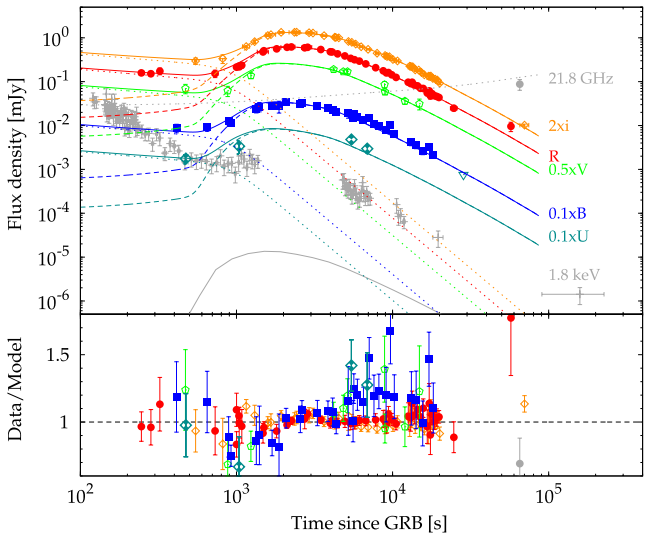

Figure 5. Top panel: light curves from radio to X-rays of the early afterglow of GRB 120404A. Here only the best sampled filters are shown together with the radio detection at 21.8 GHz. The models superposed to each data set are the synthetic light curves obtained with the BOXFIT code which best fit the corresponding data set. The continuously refreshed RS contribution (dotted line) is visible at early times, while the FS (dashed line) takes over at $t \gtrsim 10^3$ s. Bottom panel: fractional residuals.

sharp change in the temporal evolution after ∼800 s. The flux is roughly consistent with being constant with time. We first tried to characterize this emission phenomenologically. The data points covering this part are too few for fitting equation (1) with the same free parameters as used in Section 4.1. We therefore fixed the dust content to the previously determined value of $A_V = 0.22$ mag. Nevertheless, the spectral index was poorly determined as $\beta_0 = 0.6 \pm 0.6$, i.e. roughly consistent with the later value of ∼1.0. The flux density at the rest-frame frequency of 10^{15} Hz is 250^{+150}_{-90} μJy (χ^2/d.o.f. = 1.0/5).

We therefore instead tried a more physically motivated approach. One of the most natural and least ad hoc possibilities is the presence of a short-lived RS accompanying the FS. The RS is to be expected whenever given conditions are fulfilled. This is the case when the magnetization degree of the fireball σ, defined as the ratio of electromagnetic and kinetic energy density of the ejecta, is neither $\sigma < 1$ nor $\sigma > 1$ (Zhang & Kobayashi 2005). The various possible combinations of RS+FS light curves depend on the value of the synchrotron frequencies at deceleration of both shocks, $\nu_{\rm m,r}(t_{\rm d})$ and $\nu_{\rm m,f}(t_{\rm d})$, respectively, with respect to the observed frequency (Zhang, Kobayashi & Mészáros 2003; Gomboc et al. 2009; Harrison & Kobayashi 2013). In particular, in some cases the presence of a single peak or, more generally, the lack of evidence for a RS contribution, is explained in the context of the low-frequency model by relatively small microphysics parameters ϵ_e and ϵ_B which determine correspondingly small values for $\nu_{\rm m,r}$ and $\nu_{\rm m,f}$ (Mundell et al. 2007; Melandri et al. 2010; Guidorzi et al. 2011).

The value of the dimensionless parameter $\xi_0 = (l/\Delta_0)^{1/2}\,\Gamma_0^{-4/3}$ determines the evolution of the RS propagating through the ejecta, where $l = (3E_{\rm iso}/4\pi m_p\, n\, c^2)^{1/3}$ is the Sedov length, $\Delta_0 \simeq c\,T_{90}/(1+z)$ is the shell radial width in the coasting phase when it moves with a Lorentz factor Γ_0 before the deceleration sets in. From the FS modelling obtained in Section 4.3 we calculate $l = 5 \times 10^{17}$ cm. The deceleration time $t_{\rm d}$ must occur before 200 s, so it is possible to derive directly a lower limit to Γ_0,

$$t_{\rm d} = T_{90} + \frac{0.2}{\Gamma_0^{8/3}}\,\frac{l}{c}\,(1+z) < 200\ {\rm s}, \qquad (4)$$

where we used the numerical result $t_{\rm d} = (0.2 + \xi_0^{-2})\,l/c\,\Gamma_0^{8/3}$ (Harrison & Kobayashi 2013). The condition on the initial bulk Lorentz factor is $\Gamma_0 > 71$. This constrains the shell regime to be $\xi_0 < 4$, which corresponds to the intermediate/thick shell regime (Kobayashi, Piran & Sari 1999; Harrison & Kobayashi 2013).

Using this framework, we examine two possible interpretations of the early ($\lesssim$800 s) optical emission.

4.4.1 A short-lived reverse shock

If the early time emission originates from the RS emission alone, one may explain the shallow-to-steep evolution as the passage of the RS typical frequency $\nu_{\rm m,r}$ (Kobayashi 2000). In the i' band, we also see the passage of the FS component, so using these two times it is possible to infer estimates of Γ_0, of the parameter ξ_0 and of magnetization $R_{\rm B} = \epsilon_{B,\rm r}/\epsilon_{B,\rm f}$.

In the thick shell case, slow cooling regime, and frequency range $\nu < \nu_{\rm m,r}(t_{\rm d})$, after the deceleration the flux is expected to decrease with a slope of $\alpha_{\rm r,1} = 17/36$ until $\nu_{\rm m,r} \propto t^{-73/48}$ crosses the observed band, after which the slope steepens to $(73p+21)/96$ (Kobayashi 2000). We fitted the early dust-corrected $UBVRi'$ fluxes imposing the aforementioned expected temporal evolution for the flux, that for $\nu_{\rm m,r}$, the spectral slope of 1/3 at $\nu < \nu_{\rm m,r}$ (Sari, Piran & Narayan 1998), and left free to vary only two parameters, the crossing time of $\nu_{\rm m,r}$ through a given band (we chose the best sampled i'), $t_{\rm r,m,i}$, and the corresponding flux density, $F_{\rm r,m,i}$. We fitted the observed flux densities removed of the contribution of the FS as modelled with the BOXFIT code. In spite of the very few additional degrees of freedom, the result is satisfactory. The overall quality of the RS+FS model of the entire data set, excluding the X-ray band, improves to χ^2/d.o.f. = 178/129 (p-value of 0.3 per cent; Table 7), so basically equivalent to the refreshed shock modelling discussed in Section 4.4.2.

Taking $\nu_{\rm m,r}$ crossing the i' band at the fitted value of 710 s and $\nu_{\rm m,f}$ crossing at 2400 s, then we can take the typical evolutions of these frequencies ($t^{-3/2}$ and $t^{-73/48}$ for FS and RS, respectively), to estimate the ratio of frequencies at the deceleration time. This ratio has a very weak dependence on $t_{\rm d}$ due to the almost identical temporal evolution of both $\nu_{\rm m,r}$ and $\nu_{\rm m,f}$ and it is $\nu_{\rm m,r}/\nu_{\rm m,f} \simeq 0.16$. Using the numerical results by Harrison & Kobayashi (2013) and using the definition of ξ_0 one can express this ratio as a function of Γ_0 and R_B as

$$\frac{\nu_{\rm m,r}(t_{\rm d})}{\nu_{\rm m,f}(t_{\rm d})} = \left[\frac{5\times10^{-3}}{\Gamma_0^2} + \left(\frac{c\,T_{90}}{l(1+z)}\right)^{3/2}\Gamma_0^2\right] R_B^{1/2}. \qquad (5)$$

The second constraint comes from the ratio of the maximum flux densities at deceleration, $F_{\nu,\rm max,r}(t_{\rm d})/F_{\nu,\rm max,f}$ which can also be expressed as a function of Γ_0 and R_B as

$$\frac{F_{\nu,\rm max,r}(t_{\rm d})}{F_{\nu,\rm max,f}} = 0.27\left(\frac{t_{\rm d}}{710\ {\rm s}}\right)^{-1} = \frac{\Gamma_0 R_B^{1/2}}{1.5 + 5\,\xi_0^{-1.3}}, \qquad (6)$$

where $t_{\rm d}$ is given by equation (4) and $\xi_0 = (l/c\,T_{90}\,(1+z))^{1/2}\,\Gamma_0^{-4/3}$. Equation (6) is derived from numerical results (Harrison & Kobayashi 2013) and using $F_{\nu,\rm max,r} \propto t^{-1}$ (Zhang et al. 2003). From our modelling, we used $F_{\nu,\rm max,r}(710\ {\rm s}) = 0.19$ mJy and $F_{\nu,\rm max,f} = 0.7$ mJy. The solution to both equations (5) and (6) is

given by $\Gamma_0 \simeq 10^4$ and $R_B = 4.5$. In spite of the reasonable value for R_B, this scenario appears to be contrived due to the excessively high value for Γ_0. We therefore consider energy injection in addition to the RS and examine the evidence for a continuously refreshed shock.

4.4.2 *An early continuously refreshed shock*

In this scenario, we still assume that the early time emission originates in the RS, but the shallow decay phase is caused by energy injection until it switches off. The outflow profile is such that the slower moving material carries more energy in the system continuously re-energizing the ejecta as it is envisaged in the refreshed shock scenario (Sari & Mészáros 2000). We consider that the central engine launches material that has a gradient in velocity. Here the initial deceleration is similar to an impulsive fireball; however, the emission is enhanced as slower moving material catches up with decelerated material. This makes the decay of the afterglow component shallower.

From $\beta = 1.0$ we fitted early dust-corrected *UBVRi′* fluxes with the combination of the rising FS as modelled in Section 4.3 (which is negligible at $t < 800$ s) and of a continuously refreshed RS in the frequency range $\nu_{\rm m,\,r} < \nu_{\rm opt} < \nu_{\rm c,\,r}$ (Sari & Mészáros 2000). The two power-law indices were set to $\alpha_{\rm r,\,1} = (12 - 6s + 12\beta)/(2\,(7 + s))$ and $\alpha_{\rm r,\,2} = (73p + 21)/96 = 2.5$ before and after the end of the energy injection at $t_{\rm r,\,b}$, respectively (Kobayashi 2000). The free parameters adopted for the RS contribution were the normalization, the energy injection end time $t_{\rm r,\,b}$, and the velocity profile index s, $M(>\gamma) \propto \gamma^{-s}$. We derive an energy injection parameter $s = 3^{+1.5}_{-1.1}$, with energy injection ending at the observer time $t_{\rm r,\,b} = 930 \pm 400$ s (Table 7). The result is shown in Fig. 5, where the refreshed RS (RS+FS total) contribution is shown with dotted (solid) lines. In spite of the very few additional degrees of freedom, the result is satisfactory. The overall quality of the RS+FS model of the entire data set, excluding the X-ray band, improves to $\chi^2/{\rm d.o.f.} = 176/128$ (p-value of 0.3 per cent; Table 7), which is still poor, but the overall behaviour displayed by the data is modelled remarkably well. The result shows a negligible dependence on the value of the decay index $\alpha_{\rm r,\,2}$, because at $t > 800$ s the FS component dominates over the RS. This requires that the amount of energy injected is in the range 2–11 $E_{\gamma,\,\rm iso}$ and directly affects the value inferred for the radiative efficiency η_γ, which now lies in the range 0.6–0.8, i.e. higher than estimated in equation (9).

A final cross-check of this scenario is whether high-latitude emission is affected by energy injection. Although energy injection switches off at the observer time $t_{\rm r,\,b}$ s the high-latitude equivalent lab time emission could, in principle, observe energy injection at later observer times, thus affecting the FS modelling. However, the high-latitude component decays more steeply than the line-of-sight component, whose decay index is $\alpha_{\rm r,\,2} = 2.5$, making it essentially unobservable.

Therefore, in summary, we favour the continuously refreshed RS because, unlike the simple RS scenario, extreme values for Γ_0 are not required.

5 DISCUSSION

The most notable and best observed feature of GRB 120404A is the optical rebrightening peaking about 40 min after the burst, preceded by a nearly constant flux phase, which appears to be a separate component. While the optical peak is observed in a number of well-sampled early afterglows, it is generally interpreted as either (i) the afterglow onset which marks the deceleration of the ultrarelativistic ejecta by the circumburst environment or (ii) the FS radiation coming from a jet as seen from an observer outside the jet cone, i.e. when the viewing angle $\theta_{\rm obs}$ and the jet half-opening angle θ_0 are such that $\theta_{\rm obs} > \theta_0$. In the latter case, the peak in the light curve corresponds to the time at which the beaming cone widens enough to become comparable with the angle from the outer edge of the jet, i.e. when $1/\Gamma \sim (\theta_{\rm obs} - \theta_0)$ (e.g. Granot et al. 2002; Margutti et al. 2010). In the former case, the peak time is often used to estimate the initial bulk Lorentz factor at deceleration in the thin shell regime (Sari 1997), which is approximately half its value in the coasting phase preceding the deceleration (e.g. Molinari et al. 2007; Melandri et al. 2010; Liang et al. 2013; Panaitescu, Vestrand & Woźniak 2013).

A growing sample of GRBs with exquisite broad-band monitoring of the transition from the end of the prompt emission to the afterglow onset is seen to require the combination of distinct components to explain all the observations. In some cases, a double-jet configuration seems to work fairly well (e.g. Berger et al. 2003; Huang et al. 2004; Racusin et al. 2008; de Pasquale et al. 2009, 2011; Filgas et al. 2011; Holland et al. 2012). In other cases, the presence of multiple peaks is explained through the interplay between RS and FS (e.g. Zheng et al. 2012; Virgili et al. 2013, de Pasquale et al. 2013), as expected for given combinations of values for the microphysics parameters and magnetization content of the fireball (Kobayashi 2000; Zhang et al. 2003; Zhang & Kobayashi 2005).

Another possibility often discussed is that of energy injection episodes which keep refreshing the FS, whose complex behaviour would track the history of how energy is transferred to the FS as a function of time (e.g. Cucchiara et al. 2011; Rossi et al. 2011). It is not uncommon that some of the best sampled multiband afterglows require some combination of these mechanisms (Greiner et al. 2013; Virgili et al. 2013).

As for GRB 120404A, while the prompt emission lasts about 50 s, the optical flux nearly constant with time preceding the rise is detected from ∼200 to ∼800 s. An internal shock dissipation origin for this early optical emission is disfavoured because, in contrast to some GRBs with contemporaneous optical and γ-ray emission (Kopač et al. 2013), no residual γ-ray activity is detected beyond the first minute in GRB 120404A. Furthermore, the lack of temporal variability of the early optical emission argues against an internal shock dissipation origin (e.g. Nardini et al. 2011). An external origin automatically rules out the interpretation of the optical peak as due to the fireball deceleration.

Unlike the cases above which invoke a hydrodynamical origin for the peak, an alternative interpretation is that connected with the passage of the peak synchrotron frequency through the observed bands, which is chromatic (Sari et al. 1998). Although observational evidence for this was reported only for a few cases, this might be more common than what has currently been found, simply because many data sets lack well-sampled, simultaneous multicolour coverage (Oates et al. 2011; Zheng et al. 2012, de Pasquale et al. 2013).

Analogous considerations apply to the difficulty of collecting evidence for a jet break in the afterglow light curves of many GRBs (Racusin et al. 2009), whose signature can be more elusive than a clear-cut achromatic break, especially when different effects come into play simultaneously.

The high quality of the broad-band observations of GRB 120404A show the power of more comprehensive data sets for severely constraining the energetics, geometry and microphysics

parameters of the afterglow emission in conjunction with the realistic BOXFIT fitting code based on hydrodynamics simulations (van Eerten et al. 2012). As noted above, this code is applicable when most of the fireball energy has already been transferred to the ISM, so is used separately to the early time modelling of the RS emission. In the following sections, we discuss the implications derived from our modelling: in particular, implications for GRB jet geometries and the theoretical aspects of the code that could be improved to allow better modelling of the data.

5.1 The nature of the afterglow peak

The afterglow peak is the result of the passage of $\nu_{\rm m,\,f}$ through the optical bands (Zhang et al. 2003), as was the case for other exquisitely sampled GRBs (e.g. Zheng et al. 2012). To show this, we obtained two SEDs: one is measured at the peak time, the other refers to 70 ks after the burst. Fig. 6 displays the two SEDs together with the models corresponding to the set of best-fitting parameters obtained above. Noteworthy is how our radio measurements are fully consistent with the broad-band evolution and clearly show the self-absorbed regime of the synchrotron spectrum in the late SED.

The model predicts a steeper slope than that exhibited by the optical data points. This is connected with the global cooling approximation issue: due to this, the model in Fig. 6 places the cooling frequency $\nu_{\rm c,\,f}$ below the optical points, while a correct treatment of the local cooling would place it well above (see fig. 4 of van Eerten et al. 2010), thus explaining both the common spectral regime between optical and X-rays as well as the normalization of the observed X-ray flux. In this case, the need for matching the radio and the optical fluxes with a more plausible optical slope than the best-fitting model shown in Fig. 6 would require the FS peak flux density in frequency, $F_{\nu,\,\rm max,\,f}$, to decrease with time. However, this clashes with the $F_{\nu,\,\rm max,\,f} \propto t^0$ evolution expected in the homogeneous medium scenario assumed by the BOXFIT code. For a wind density profile, it is $F_{\nu,\,\rm max,\,f} \propto t^{-1/2}$ (Chevalier & Li 1999). In Section 4.2, we argued that a wind-like density profile is not ruled out from the expected closure relation at late times. This suggests that a local cooling treatment combined with the possibility of wind-like environments could help to improve the modelling capabilities of the BOXFIT code. A repeat run *without* cooling modelled the optical slope slightly better, but did not improve the quality of the overall fit and caused a significantly worse fit to the radio data. This therefore further confirms the need for a code development to include more realistic cooling and density profiles.

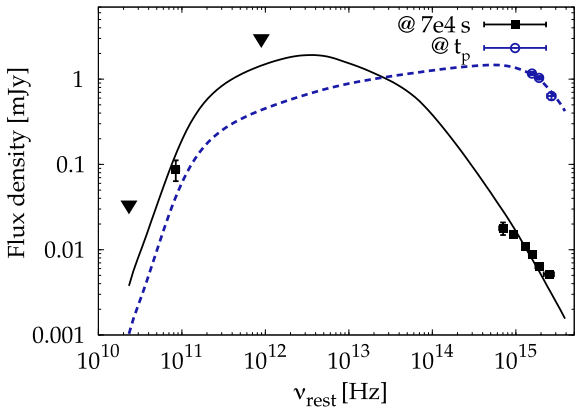

Figure 6. Rest-frame SEDs at peak (circles and dashed line) and at 70 ks (squares and solid lines) including radio and optical measurements. Optical points have been corrected for dust extinction using $A_V = 0.22$ mag for a MW profile. Upside-down triangles are 3σ upper limits. The thick solid line shows the best-fitting model based on hydrodynamical simulations.

5.2 An edge-on view of a wide jet

Excluding the X-ray data, the best-fitting parameters do not change in essence and confirm the basic picture of a relatively wide jet viewed from a direction close to the edge but still inside the jet cone. Although the true θ_0 distribution is difficult to derive from observations because of the numerous selection effects and observational biases (Bloom, Frail & Kulkarni 2003; Lu et al. 2012), past data suggest the existence of comparably wide jets (Bloom et al. 2003; Fong et al. 2012), as clearly shown in Fig. 7 which displays the θ_0 distribution for a number of *Swift* long GRBs. The FS microphysics parameters are within the range of typical values estimated for other GRBs (Panaitescu & Kumar 2002), apart from the high value of p, which is likely to be connected with the aforementioned global cooling issue. The ISM particle density n is high, but still within the high tail of the distribution.

The quality of the data set, combined with the capability of the fitting code, allowed us to constrain both θ_0 and $\theta_{\rm obs}$, as shown by Fig. 8, which compares the observed data and model with what an

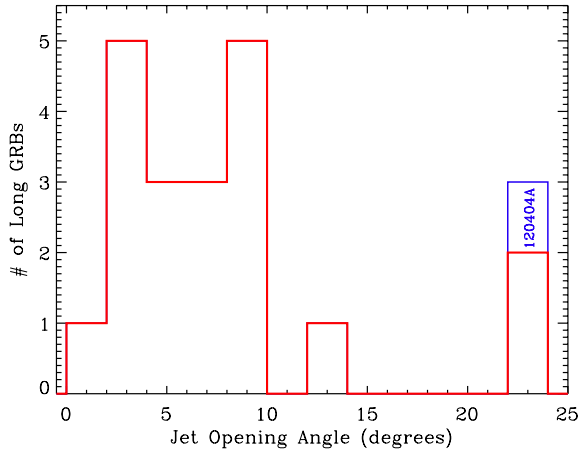

Figure 7. Jet half-opening angle distribution for a number of *Swift* long GRBs. GRB 120404A lies in the wide-angle tail.

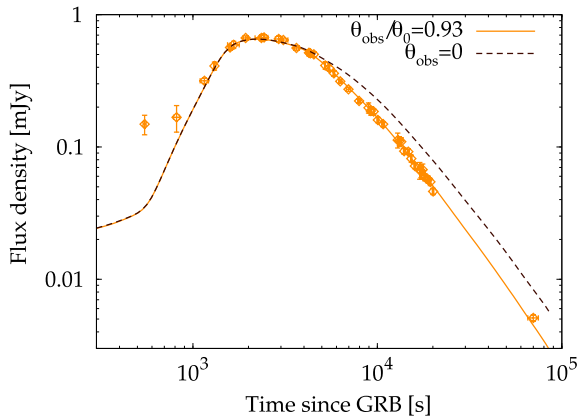

Figure 8. Light curve in the i' band. The solid line shows the best-fitting solution obtained for a jet opening angle $\theta_0 = 23^\circ$ and viewing angle $\theta_{\rm obs} = 21^\circ$. The dashed line shows what an on-axis observer would have observed for the same GRB.

on-axis observer would have observed. The accurately modelled shape of the multiband light curves is sensitive to the missing flux from the jet edge closer to the observer sightline, when $1/\Gamma \sim (\theta_0 - \theta_{\rm obs})$. The time at which this is observed can be clearly estimated from Fig. 8 around $t_{j,1} \simeq 5$ ks, and corresponds to

$$\theta_0 - \theta_{\rm obs} = 2.7^\circ \left(\frac{t_{j,1}\,\zeta}{5\ {\rm ks}}\right)^{3/8} \left(\frac{n_0}{244}\right)^{1/8} \left(\frac{E_{\rm iso,53}}{1.9}\right)^{-1/8}, \quad (7)$$

as expected from the corresponding best-fitting values ($\zeta = 3.876/(1+z)$). One should expect to also see the final and steep drop in the decay slope associated with the further jet edge, i.e. when it is $\Gamma \sim 1/(\theta_0 + \theta_{\rm obs})$. This is to be expected at the time $t_{j,2}$

$$t_{j,2} = \left(\frac{\theta_0 + \theta_{\rm obs}}{\theta_0 - \theta_{\rm obs}}\right)^{8/3} t_{j,1} \simeq 100\ {\rm d}, \quad (8)$$

which is far beyond the coverage of our data set.

Another interesting result from the afterglow modelling is the possibility to constrain the radiative efficiency η_γ of the prompt emission (Zhang et al. 2007),

$$\eta_\gamma = \frac{E_{\gamma,{\rm iso}}}{E_{\rm iso} + E_{\gamma,{\rm iso}}} = 0.3 \pm 0.1\,, \quad (9)$$

which is consistent with typical expectations from internal shocks (Beloborodov 2000; Guetta, Spada & Waxman 2001; Kobayashi & Sari 2001) as well as with values measured for other GRBs (Zhang et al. 2007). However, the value of 0.3 for η_γ becomes a lower limit if the early optical emission is due to prolonged internal activity, such as the case considered in Section 4.4.2. It is also possible to calculate the total kinetic energy corrected for collimation,

$$E_{\rm K} = E_{\rm iso}\,(1 - \cos\theta_0) = 1.5 \times 10^{52}\ {\rm erg}. \quad (10)$$

In addition to the global cooling approximation issue, other limitations of the BOXFIT code concern the jet angular structure, assumed to be homogeneous with sharp boundaries, as well as the assumption of a homogeneous instead of a wind-like density profile of the surrounding medium, as argued in Section 5.1. Adopting more realistic jet structures can possibly lead to further improvements in the data modelling (e.g. Rossi, Lazzati & Rees 2002; Zhang & Mészáros 2002; Zhang et al. 2004; Granot 2005; Guetta, Granot & Begelman 2005; Panaitescu & Vestrand 2008).

6 CONCLUSIONS

We presented the first high-quality broad-band data set of a GRB fitted with a realistic code developed and made available by van Eerten et al. (2012). This code was built upon hydrodynamical simulations and not merely on analytical approximations, to model the afterglow evolution from radio to high energies. In particular, we found that synchrotron radiation expected from the FS propagating through a constant medium within the shape of a homogeneous jet with opening angle $\theta_0 = 23.1^{+0.8}_{-4.1}$ degrees viewed almost edge-on, $\theta_{\rm obs} = (0.93 \pm 0.01)\,\theta_0$ can reproduce very accurately the well-sampled multiband light curves of GRB 120404A.

We constrained the microphysics of the relativistic shock, which gives rise to the FS emission and a posteriori highlights the importance of adopting a local cooling treatment in place of the commonly adopted global cooling in modelling the flux above the cooling break. These results unambiguously suggest that future theoretical developments and refinements of models like the one we adopted here should provide a more realistic description of the local cooling and its impact at high energies, and should also include wind-like density profiles in addition to the already treated homogeneous case.

The optical peak observed a few thousands seconds after the burst, which is a common property among many GRB early afterglows, shows evidence for a chromatic character and is satisfactorily explained by the crossing of the FS synchrotron peak frequency $\nu_{\rm m,f}$ through the observed bands. This exclude the interpretation of the peak as the time of fireball deceleration, which appears to be contrived due to the initial constant optical flux density,[7] and highlight the need for caution in automatically interpreting all optical peaks as deceleration signatures.

We instead successfully modelled the same early optical emission in terms of a RS which is continuously refreshed by a velocity distribution of the ejecta for about 10^3 s after the burst. The fireball deceleration occurs in the intermediate/thick shell regime and highlights the importance of correct treatment to evaluate the relative strength between forward and RS emission to constrain the fireball magnetization and the initial bulk Lorentz factor (Harrison & Kobayashi 2013).

The total released isotropic-equivalent and collimation-corrected energy, $\sim 2 \times$ and $\sim 0.1 \times 10^{53}$ erg respectively, allowed us to directly estimate the radiative efficiency of the prompt emission, which is found to be either $\eta_\gamma = 0.7 \pm 0.15$ or $\eta_\gamma = 0.3 \pm 0.1$, depending on whether the early optical emission is the result or not of prolonged energy injection into the fireball.

Our capability of constraining the jet geometry provides new insight into the long-standing difficulty of measuring clear-cut jet breaks for GRBs in the *Swift* era and emphasizes the role played by an off-axis angle when this is comparable to the jet opening angle. Moreover, our results add strong support for the growing evidence that comparably wide jets as viewed from comparably large off-axis directions are probably more common than previously inferred from simple analytical descriptions (Ryan, van Eerten & MacFadyen 2013).

Overall, the entire data set is well explained with a combination of reverse and FS in a relatively wide homogeneous jet viewed nearly edge-on plus energy injection. This seems to be a natural choice in other GRBs similar to GRB 120404A, in which the prompt emission is characterized by a very simple FRED.

ACKNOWLEDGEMENTS

CG acknowledges ASI for financial support (ASI-INAF contract I/088/06/0) and University of Ferrara for use of the local HPC facility co-funded by the 'Large-Scale Facilities 2010' project (grant 7746/2011). CG thanks Hendrik van Eerten for useful discussions. CGM thanks the Royal Society, Wolfson Foundation and Science and Technology Facilities Council for support. EB and BAZ were supported in part by the National Science Foundation under Grant AST-1107973. BAZ is supported by an NSF Astronomy and Astrophysics Postdoctoral Fellowship under award AST-1302954. AG acknowledges founding from the Slovenian Research Agency and from the Centre of Excellence for Space Sciences and Technologies SPACE-SI, an operation partly financed by the European Union, the European Regional Development Fund and the Republic of Slovenia, Ministry of Education, Science and Sport.

[7] To be explained in terms of fireball deceleration, it would require a non-uniform shell with the innermost part carrying a significant fraction of the shell energy, so that the ISM would receive a major impulsive energy injection at the end of the RS crossing.

Development of the Boxfit code was supported in part by NASA through grant NNX10AF62G issued through the Astrophysics Theory Programme and by the NSF through grant AST-1009863. The NRAO is a facility of the NSF operated under cooperative agreement by AUI. Proposal VLA 12A-394 is acknowledged. The SMA is a joint project between SAO and the ASIAA and is funded by the Smithsonian Institution and the Academia Sinica. Part of the funding for GROND (both hardware as well as personnel) was generously granted from the Leibniz-Prize to Professor G. Hasinger (DFG grant HA 1850/28-1). We thank the anonymous referee for helpful comments that improved the paper.

REFERENCES

Barthelmy S. D. et al., 2005, Space Sci. Rev., 120, 143
Beloborodov A. M., 2000, ApJ, 539, L25
Berger E. et al., 2003, Nature, 426, 154
Blandford R. D., McKee C. F., 1976, Phys. Fluids, 19, 1130
Bloom J. S., Frail D. A., Kulkarni S. R., 2003, ApJ, 594, 674
Breeveld A. A., Stratta G., 2012, GRB Coordinates Network, 13226, 1
Burrows D. N. et al., 2005, Space Sci. Rev., 120, 165
Campana S. et al., 2012, MNRAS, 421, 1697
Cardelli J. A., Clayton G. C., Mathis J. S., 1989, ApJ, 345, 245
Chevalier R. A., Li Z.-Y., 1999, ApJ, 520, L29
Covino S. et al., 2010, A&A, 521, A53
Cucchiara A., Tanvir N. R., 2012, GRB Coordinates Network, 13217, 1
Cucchiara A. et al., 2011, ApJ, 743, 154
D'Elia V., Goldoni P., Malesani D., Tanvir N. R., Fynbo J. P. U., Melandri A., 2012, GRB Coordinates Network, 13227, 1
de Pasquale M. et al., 2009, MNRAS, 392, 153
de Pasquale M. et al., 2011, Adv. Space Res., 48, 1411
de Pasquale M. et al., 2013, MNRAS, submitted
Dougherty S. M., Perley R. A., 2010, in Kothes R., Landecker T. L., Willis A. G., eds, ASP Conf. Ser. Vol. 438, The Dynamic Interstellar Medium: A Celebration of the Canadian Galactic Plane Survey. Astron. Soc. Pac., San Francisco, p. 421
Evans P. A. et al., 2009, MNRAS, 397, 1177
Filgas R. et al., 2011, A&A, 526, A113
Fong W. et al., 2012, ApJ, 756, 189
Fukugita M., Shimasaku K., Ichikawa T., 1995, PASP, 107, 945
Fukugita M., Ichikawa T., Gunn J. E., Doi M., Shimasaku K., Schneider D. P., 1996, AJ, 111, 1748
Fynbo J. P. U. et al., 2009, ApJS, 185, 526
Fynbo J. P. U., Malesani D., Jakobsson P., 2012, in Kouveliotou C., Wijers R. A. M. J., Woosley S., eds, Gamma-Ray Bursts. Cambridge Univ. Press, Cambridge, p. 269
Gao H., Lei W.-H., Zou Y.-C., Wu X.-F., Zhang B., 2013, New Astron. Rev., 57, 141
Gehrels N., Mészáros P., 2012, Science, 337, 932
Gendre B. et al., 2010, MNRAS, 405, 2372
Gomboc A. et al., 2009, in Meegan C., Kouveliotou C., Gehrels N., eds, AIP Conf. Ser. Vol. 1133, Optical Flashes, Reverse Shocks and Magnetization. Am. Inst. Phys., New York, p. 145
Granot J., 2005, ApJ, 631, 1022
Granot J., Panaitescu A., Kumar P., Woosley S. E., 2002, ApJ, 570, L61
Greiner J. et al., 2008, PASP, 120, 405
Greiner J. et al., 2011, A&A, 526, A30
Greiner J. et al., 2013, preprint (arXiv:1304.5852)
Greisen E. W., 2003, in Heck A., ed., Information Handling in Astronomy - Historical Vistas, Kluwer, Dordrecht, p. 109
Guetta D., Spada M., Waxman E., 2001, ApJ, 557, 399
Guetta D., Granot J., Begelman M. C., 2005, ApJ, 622, 482
Guidorzi C. et al., 2006, PASP, 118, 288
Guidorzi C. et al., 2009, A&A, 499, 439
Guidorzi C. et al., 2011, MNRAS, 417, 2124
Guidorzi C., Melandri A., Japelj J., 2012, GRB Coordinates Network, 13209, 1
Harrison R., Kobayashi S., 2013, ApJ, 772, 101
Ho P. T. P., Moran J. M., Lo K. Y., 2004, ApJ, 616, L1
Holland S. T. et al., 2012, ApJ, 745, 41
Hook I. M., Jørgensen I., Allington-Smith J. R., Davies R. L., Metcalfe N., Murowinski R. G., Crampton D., 2004, PASP, 116, 425
Huang Y. F., Wu X. F., Dai Z. G., Ma H. T., Lu T., 2004, ApJ, 605, 300
Jin Z. P., Fan Y. Z., 2007, MNRAS, 378, 1043
Jordi K., Grebel E. K., Ammon K., 2006, A&A, 460, 339
Kalberla P. M. W., Burton W. B., Hartmann D., Arnal E. M., Bajaja E., Morras R., Pöppel W. G. L., 2005, A&A, 440, 775
Kaneko Y., Preece R. D., Briggs M. S., Paciesas W. S., Meegan C. A., Band D. L., 2006, ApJS, 166, 298
Kobayashi S., 2000, ApJ, 545, 807
Kobayashi S., Sari R., 2001, ApJ, 551, 934
Kobayashi S., Piran T., Sari R., 1999, ApJ, 513, 669
Kopač D. et al., 2013, ApJ, 772, 73
Krühler T. et al., 2009, A&A, 508, 593
Kumar B., Bhatt V. K., Pandey S. B., 2012, GRB Coordinates Network, 13234, 1
Liang E.-W. et al., 2013, ApJ, 774, 13
Lu R.-J., Wei J.-J., Qin S.-F., Liang E.-W., 2012, ApJ, 745, 168
Margutti R. et al., 2010, MNRAS, 402, 46
Margutti R. et al., 2013, MNRAS, 428, 729
Melandri A. et al., 2008, ApJ, 686, 1209
Melandri A. et al., 2010, ApJ, 723, 1331
Mészáros P., 2006, Rep. Prog. Phys., 69, 2259
Molinari E. et al., 2007, A&A, 469, L13
Morrison R., McCammon D., 1983, ApJ, 270, 119
Mundell C. G. et al., 2007, ApJ, 660, 489
Nardini M. et al., 2011, A&A, 531, A39
Norris J. P., Nemiroff R. J., Bonnell J. T., Scargle J. D., Kouveliotou C., Paciesas W. S., Meegan C. A., Fishman G. J., 1996, ApJ, 459, 393
Norris J. P., Bonnell J. T., Kazanas D., Scargle J. D., Hakkila J., Giblin T. W., 2005, ApJ, 627, 324
Oates S. R. et al., 2011, MNRAS, 412, 561
Osborne J. P., Beardmore A. P., Evans P. A., Goad M. R., 2012, GRB Coordinates Network, 13218, 1
Panaitescu A., Kumar P., 2002, ApJ, 571, 779
Panaitescu A., Vestrand W. T., 2008, MNRAS, 387, 497
Panaitescu A., Vestrand W. T., Woźniak P., 2013, MNRAS, 433, 759
Pei Y. C., 1992, ApJ, 395, 130
Perley D. A. et al., 2009, AJ, 138, 1690
Perley R. A., Chandler C. J., Butler B. J., Wrobel J. M., 2011, ApJ, 739, L1
Prochaska J. X., Chen H.-W., Bloom J. S., 2006, ApJ, 648, 95
Racusin J. L. et al., 2008, Nature, 455, 183
Racusin J. L. et al., 2009, ApJ, 698, 43
Roming P. W. A. et al., 2005, Space Sci. Rev., 120, 95
Roming P. W. A. et al., 2006, ApJ, 652, 1416
Rossi E., Lazzati D., Rees M. J., 2002, MNRAS, 332, 945
Rossi A. et al., 2011, A&A, 529, A142
Ryan G., van Eerten H., MacFadyen A., 2013, preprint (arXiv:1307.6334)
Sakamoto T. et al., 2009, ApJ, 693, 922
Sakamoto T. et al., 2011, ApJS, 195, 2
Sari R., 1997, ApJ, 489, L37
Sari R., Mészáros P., 2000, ApJ, 535, L33
Sari R., Piran T., Narayan R., 1998, ApJ, 497, L17
Savaglio S., 2012, EAS Publ. Ser., 61, 381
Schlegel D. J., Finkbeiner D. P., Davis M., 1998, ApJ, 500, 525
Spergel D. N. et al., 2003, ApJS, 148, 175
Spitkovsky A., 2008, ApJ, 682, L5
Stratta G. et al., 2012, GRB Coordinates Network, 13208, 1
Sudilovsky V., Rau A., Greiner J., 2012, GRB Coordinates Network, 13229, 1
Tristram P. J., Fukui A., Sako T., 2012, GRB Coordinates Network, 13228, 1
Ukwatta T. N. et al., 2012, GRB Coordinates Network, 13220, 1
van Dokkum P. G., 2001, PASP, 113, 1420
van Eerten H., 2013, preprint (arXiv:1309.3869)

van Eerten H., Zhang W., MacFadyen A., 2010, ApJ, 722, 235
van Eerten H., van der Horst A., MacFadyen A., 2012, ApJ, 749, 44
Vernet J. et al., 2011, A&A, 536, A105
Virgili F. J. et al., 2013, ApJ, 778, 54
Vreeswijk P. M. et al., 2007, A&A, 468, 83
Yost S. A. et al., 2007a, ApJ, 657, 925
Yost S. A. et al., 2007b, ApJ, 669, 1107
Zauderer A., Laskar T., Berger E., 2012, GRB Coordinates Network, 13231, 1
Zauderer B. A. et al., 2013, ApJ, 767, 161
Zhang B., Kobayashi S., 2005, ApJ, 628, 315
Zhang B., Mészáros P., 2002, ApJ, 571, 876
Zhang B., Kobayashi S., Mészáros P., 2003, ApJ, 595, 950
Zhang B., Dai X., Lloyd-Ronning N. M., Mészáros P., 2004, ApJ, 601, L119
Zhang B. et al., 2007, ApJ, 655, 989
Zheng W. et al., 2012, ApJ, 751, 90

This paper has been typeset from a TEX/LATEX file prepared by the author.